Journal of Computational Physics: X 8 (2020) 100070

Contents lists available at ScienceDirect

Journal of Computational Physics: X

www.elsevier.com/locate/jcpx

# Heterogeneous multiscale method for high energy-density matter: Connecting kinetic theory and molecular dynamics

Gil Shohet [a,*], Jacob Price [b,1], Jeffrey Haack [c], Mathieu Marciante [c,2], Michael S. Murillo [d]

[a] Department of Aeronautics and Astronautics, Stanford University, Stanford, CA 94305, USA
[b] Department of Applied Mathematics, University of Washington, Seattle, WA 98195, USA
[c] Computational Physics and Methods Group, Los Alamos National Laboratory, Los Alamos, NM 87545, USA
[d] Department of Computational Mathematics, Science and Engineering, Michigan State University, East Lansing, MI 48824, USA

ARTICLE INFO

*Article history:*
Received 19 July 2019
Received in revised form 5 May 2020
Accepted 10 August 2020
Available online 17 August 2020

*Keywords:*
Plasma modeling
Multiscale
Kinetic theory
Molecular dynamics
Heterogeneous multiscale method

ABSTRACT

We have developed a concurrent heterogeneous multiscale method (HMM) framework with a microscale molecular dynamics (MD) model and a macroscale kinetic Vlasov-BGK model. The kinetic model is formulated such that BGK collision times are the closure data obtained from MD. Using the H-theorem, we develop the mathematical link between the MD and the kinetic model. We examine three relaxation processes, energy, momentum, and bump-on-tail, using full microscale MD simulations as a reference solution. We find that solutions computed with the HMM framework offer a significant computational reduction ($14\times - 100\times$) compared with computing a full MD solution, with significant improvements in accuracy compared with a kinetic model using analytical collision times.


## 1. Introduction

Nearly all applications in science and engineering involve processes that occur at disparate time and length scales, ranging from microscopic quantum processes to macroscale thermodynamic processes. When modeling at the largest scales, precomputed microscopic data serves as the closure for the macroscopic model. For example, the required microscopic closure data for hydrodynamics are an equation of state and, for the Navier-Stokes equations, transport coefficients. Typically, such data are available in the form of tables or fitting functions. For kinetic models, which describe plasmas or gases that are out of thermal equilibrium, the microscopic closures are e.g. collision rates or cross sections, depending on the kinetic model employed [1–7]. Such models can be used to model, for example, inertial-confinement fusion (ICF), where effects such as fuel isotopic separation [8–10] and shell-fuel mixing [11–17] cannot be described by hydrodynamics.

Precomputing microscopic closure information works well when the macroscopic fields vary over predictable ranges and when the dimensionality of the closure input data is not large. However, modeling complex mixtures requires knowing in advance which mixtures might form, and under what conditions. Additionally, traditional models for computing microscopic closures rely on assumptions, e.g. weak coupling in plasmas, that are not valid in many applications of interest. To avoid

* Corresponding author.
*E-mail addresses:* shohet@stanford.edu (G. Shohet), jrprice@pugetsound.edu (J. Price), haack@lanl.gov (J. Haack), mathieu.marciante@cea.fr (M. Marciante), murillom@msu.edu (M.S. Murillo).
[1] Present address: Department of Mathematics and Computer Science, University of Puget Sound, Tacoma, WA 98416, USA.
[2] Present address: CEA-DAM, DIF F-91297 Arpajon, France.

https://doi.org/10.1016/j.jcpx.2020.100070

the need to model the entire high-dimensional microscale parameter space, concurrent multiscale approaches employ two or more distinct computational models simultaneously at different scales [18,19].

Concurrent multiscale approaches provide a means to model systems for which neither microscopic nor macroscopic models alone are sufficiently computationally efficient or accurate. The heterogeneous multiscale method (HMM) capitalizes on temporal and spatial scale separation to increase the accuracy of a macroscale model using data drawn from a microscale model that runs concurrently [20,21]. Such multimodel approaches can be developed using partitioned domain methods, in which different models operate in separate spatial domains, or with time-split approaches in which the two models are used alternatingly across different time intervals. Hybrid kinetic-molecular dynamics (MD) models, which are not strictly HMM models, have been developed to model ultracold neutral plasmas [22] and hot dense plasmas [23,24]. The HMM has been successfully applied to gas dynamics problems using MD to compute hydrodynamic fluxes [21,25], dynamic crack propagation [26] and heat conduction in fine-scale structures [27]. Multiscale domain decomposition methods have been used in neutral-gas kinetic problems to couple a local kinetic Boltzmann model to the Navier-Stokes equations to model hypersonic flows [28]. However, to our knowledge, MD has never been coupled to a kinetic equation using the HMM.

In this paper, we describe a multiscale kinetic-MD model based on the HMM framework. In this model, the relaxation times used in the multispecies Vlasov-Bhatnagar-Gross-Krook (VBGK) kinetic model are computed from MD simulations on a small subset of the physical domain of interest. The result is an adaptive, hybrid simulation method that employs MD-accurate relaxation times to significantly improve the accuracy of the VBGK model, while requiring significantly less computational time than would be required for a full MD simulation. The multiscale coupling between the models is handled through a middleware layer that interfaces between the MD and kinetic codes. In Section 2, we specify the VBGK and MD models and their mathematical connection. In Section 3, we present the HMM model that links these two models, and we describe the procedure for generating collision rates for the kinetic model from the MD results, the criteria that the kinetic model uses to update its microscopic information, and initialization details for the MD simulations. In Section 4, we describe the simulation details and present validation results, which demonstrate the improvement in accuracy over a VBGK model without coupling to MD. In Section 5, we summarize our results and propose further extensions of the model, as well as potential applications.

## 2. Data linkage between molecular dynamics and kinetic models

HMM models contain a macroscale model for which missing closure information is obtained from a microscale model. For example, a hydrodynamic macroscale model would provide constraints of temperature and density, under which the microscale model provides the stress tensor. In this paper, we extend this notion to kinetic systems, that is, systems that are not near thermodynamic equilibrium.

In plasma systems for which microscopic effects are important, MD is the natural model for both theory and simulations [29–31]; however, the utility of MD is limited by the maximum system size [32]. State-of-the-art MD simulations can evolve $N = O(10^{12})$-particle systems; such systems correspond to physical domains on the order of several $\mu m^3$ [33]. However, this physical size is much smaller than, e.g., the size of an ICF capsule. Furthermore, MD can probe time scales typically on the order of only picoseconds to microseconds, and it poses an additional challenge in that calculations can produce tens of terabytes of data per time step [34].

Kinetic theory (KT) describes the statistical evolution of single-particle distributions $f(\mathbf{r}, \mathbf{v}, t)$ in phase space, which can model larger time and space scales than MD. Kinetic models describe nonequilibrium phenomena, and their applicability can be quantified by the Knudsen number $\mathcal{K}$, which is the ratio of the mean-free path between particle collisions and a characteristic length scale of the system. For very small Knudsen numbers, collisions drive the system to equilibrium very quickly, and hydrodynamic models are sufficient to describe the dynamics of the system. However, for $\mathcal{K} \gtrsim 0.1$, the assumptions of hydrodynamics begin to break down and a kinetic model is necessary. A generic microscopic closure for a kinetic model is the two-particle distribution function $f_2(\mathbf{r}, \mathbf{v}, \mathbf{r}', \mathbf{v}', t)$ in the BBGKY hierarchy. Specific assumptions on the form of $f_2$ lead to kinetic models such as Boltzmann, for which the cross section incorporates the microscopic data, or the Bhatnagar-Gross-Krook model, for which the collision rates are the closure data. This generic $f_2$ function is at least four dimensional and is, in general, 12 dimensional, and simply storing the information in $f_2(\mathbf{r}, \mathbf{v}, \mathbf{r}', \mathbf{v}', t)$ would require an excessive amount of memory. For this reason, we seek an alternate, more manageable coupling strategy. In order to develop an HMM that connects the kinetic and MD representations of the same system, we derive the multispecies VBGK kinetic equation from the microscopic Hamiltonian dynamics.

Consider a classical multispecies plasma mixture comprising ions with charges $Z_k e$ at densities $n_k$ with masses $m_k$ that interact through a pair potential $U_{kl}$. We define $U_{kl}(\mathbf{r}, \mathbf{r}) = 0$ for later convenience, recognizing that particles cannot exactly overlap. This system evolves according to the Hamiltonian

$$H = \sum_i \left( \frac{m_i |\mathbf{v}_i|^2}{2} + \frac{1}{2} \sum_{j \neq i} U_{kl}(\mathbf{r}_i, \mathbf{r}_j) \right), \tag{1}$$

where $(\mathbf{r}_i(t), \mathbf{v}_i(t))$ is the position and velocity of particle $i$ at time $t$, $i$ is a particle of species $k$, and $j$ is a particle of species $l$.

To derive a kinetic equation from this particle system, we begin by constructing a Klimontovich distribution [35] $N_k$ for each species $k$ that gives the location $\mathbf{r}_i$ and velocity $\mathbf{v}_i$ of every particle of that species at a given time $t$:

$$N_k(\mathbf{r},\mathbf{v},\{\mathbf{r}_\alpha\}_{\alpha=1}^N,\{\mathbf{v}_\alpha\}_{\alpha=1}^N,t)=\sum_{i\in S_k}\delta\left(\mathbf{r}-\mathbf{r}_i\right)\delta\left(\mathbf{v}-\mathbf{v}_i\right). \tag{2}$$

Here, $\delta(x)$ is the Dirac delta function, and $S_k$ is the set of ion indices corresponding to species $k$. The ensemble expected value of $N_k$ is the definition of the velocity distribution function $f_k$:

$$f_k(\mathbf{r},\mathbf{v},t)\equiv\langle N_k\rangle. \tag{3}$$

This ensemble average is taken with respect to all initial choices for $\mathbf{r}_i(0)$ and $\mathbf{v}_i(0)$ consistent with the initial distributions $f_k(\mathbf{r},\mathbf{v},0)$. This defines the ensemble over which we consider each average. Taking the time derivative of $N_k$, we have

$$\frac{\partial N_k}{\partial t}=\sum_{i\in S_k}\frac{\partial}{\partial t}\delta(\mathbf{r}-\mathbf{r}_i)\delta(\mathbf{v}-\mathbf{v}_i) \tag{4}$$

$$=\sum_{i\in S_k}\left\{\delta(\mathbf{v}-\mathbf{v}_i)\frac{\partial}{\partial t}\delta(\mathbf{r}-\mathbf{r}_i)+\delta(\mathbf{r}-\mathbf{r}_i)\frac{\partial}{\partial t}\delta(\mathbf{v}-\mathbf{v}_i)\right\} \tag{5}$$

$$=\sum_{i\in S_k}\left\{-\frac{\partial\mathbf{r}_i(t)}{\partial t}\delta(\mathbf{v}-\mathbf{v}_i)\cdot\nabla_{\mathbf{r}}\delta(\mathbf{r}-\mathbf{r}_i)-\frac{\partial\mathbf{v}_i}{\partial t}\delta(\mathbf{r}-\mathbf{r}_i)\cdot\nabla_{\mathbf{v}}\delta(\mathbf{v}-\mathbf{v}_i)\right\}. \tag{6}$$

We can now substitute the Hamiltonian equations for the evolution of $\mathbf{r}_i$ and $\mathbf{v}_i$ into (6), obtaining

$$\frac{\partial N_k}{\partial t}=\sum_{i\in S_k}\left\{-\mathbf{v}_i\delta(\mathbf{v}-\mathbf{v}_i)\cdot\nabla_{\mathbf{r}}\delta(\mathbf{r}-\mathbf{r}_i)+\frac{1}{m_k}\delta(\mathbf{r}-\mathbf{r}_i)\times\nabla_{\mathbf{r}_i}\left(\sum_l\sum_{\substack{j\in S_l\\ j\neq i}}U_{kl}(\mathbf{r}_i,\mathbf{r}_j)\right)\cdot\nabla_{\mathbf{v}}\delta(\mathbf{v}-\mathbf{v}_i)\right\}. \tag{7}$$

Because $\mathbf{v}_i\delta(\mathbf{v}-\mathbf{v}_i)$ is only nonzero when $\mathbf{v}=\mathbf{v}_i$, we find

$$\mathbf{v}_i\delta(\mathbf{v}-\mathbf{v}_i)=\mathbf{v}\delta(\mathbf{v}-\mathbf{v}_i). \tag{8}$$

A similar relation holds for the second term. Using this and simplifying, we find

$$\frac{\partial N_k}{\partial t}=-\mathbf{v}\cdot\nabla_{\mathbf{r}}N_k+\frac{1}{m_k}\nabla_{\mathbf{r}}\left(\sum_l\sum_{j\in S_l}U_{kl}(\mathbf{r},\mathbf{r}_j)\right)\cdot\nabla_{\mathbf{v}}N_k. \tag{9}$$

We now take the ensemble average of both sides of (9) and obtain

$$\frac{\partial f_k}{\partial t}=-\mathbf{v}\cdot\nabla_{\mathbf{r}}f_k+\frac{1}{m_k}\left\langle\nabla_{\mathbf{r}}\left(\sum_l\sum_{j\in S_l}U_{kl}(\mathbf{r},\mathbf{r}_j)\right)\cdot\nabla_{\mathbf{v}}N_k\right\rangle. \tag{10}$$

To simplify the second term in (10), we use the definition of $N_l$,

$$\sum_{j\in S_l}U_{kl}(\mathbf{r},\mathbf{r}_j)=\int U_{kl}(\mathbf{r},\mathbf{r}')N_l(\mathbf{r}',\mathbf{v}',t)\,\mathrm{d}\mathbf{r}'\mathrm{d}\mathbf{v}', \tag{11}$$

to obtain

$$\left\langle\nabla_{\mathbf{r}}\left(\sum_l\sum_{j\in S_l}U_{\{kl\}}(\mathbf{r},\mathbf{r}_j)\right)\cdot\nabla_{\mathbf{v}}N_k\right\rangle=\sum_l\int\nabla_{\mathbf{r}}U_{kl}(\mathbf{r},\mathbf{r}')\cdot\nabla_{\mathbf{v}}\left\langle N_k(\mathbf{r},\mathbf{v})N_l(\mathbf{r}',\mathbf{v}')\right\rangle\mathrm{d}\mathbf{r}'\mathrm{d}\mathbf{v}'. \tag{12}$$

The product of two Klimontovich distribution functions is the two-species Klimontovich distribution function for that species pair, $N_{kl}(\mathbf{r},\mathbf{v},\mathbf{r}',\mathbf{v}',\{\mathbf{r}_k\}_{k=1}^n,\{\mathbf{v}_k\}_{k=1}^n,t)$. The expected value of the Klimontovich distribution function is the two-species distribution function $f_{kl}$:

$$f_{kl}(\mathbf{r},\mathbf{v},\mathbf{r}',\mathbf{v}',t)\equiv\langle N_{kl}\rangle. \tag{13}$$

This introduces a new, unknown function $f_{kl}$, which we need to write in terms of the one particle distribution functions $f_k$, $f_l$ in order to close the equations. Because the two-particle distribution function can be written as the product of two one-particle distribution functions when the two species are not correlated, we write $f_{kl}$, without loss of generality, as

$$f_{kl}(\mathbf{r},\mathbf{v},\mathbf{r}',\mathbf{v}',t) = f_k(\mathbf{r},\mathbf{v},t)f_l(\mathbf{r}',\mathbf{v}',t) + C_{kl}, \tag{14}$$

where $C_{kl}$ contains correlations beyond the mean-field approximation. This decomposition can be thought of as separating interactions into mean-field interactions and deviations from the mean field. Substitution of this approximation into (12) yields

$$\left\langle \nabla_{\mathbf{r}} \left( \sum_l \sum_{j\in S_l} U_{kl}(\mathbf{r},\mathbf{r}_j) \right) \cdot \nabla_{\mathbf{v}} \langle N_k \rangle \right\rangle = \nabla_{\mathbf{r}} \sum_l \left( \int U_{kl}(\mathbf{r},\mathbf{r}') n_l(\mathbf{r}',t)\, \mathrm{d}\mathbf{r}' \right) \cdot \nabla_{\mathbf{v}} f_k + C'_{kl}, \tag{15}$$

where $C'_{kl}$ is another remainder term.

To proceed further, we need to specify the interparticle forces. In the context of plasmas, in principle, it is possible to include the electrons as one of the dynamical species; however, because the electron mass is much less than the ion mass, we will assume that the electrons follow the ions adiabatically, producing an average density of

$$n_e(\mathbf{r}) = n_e^0 + \Delta n_e(\mathbf{r}), \tag{16}$$

where $n_e^0$ is the global average electron density, and $\Delta n_e(\mathbf{r})$ are linear screening electron clouds that follow ions throughout the domain. The effects of these electron clouds are captured in MD by employing the Yukawa potential between ions,

$$U_{kl}(\mathbf{r},\mathbf{r}') = \frac{Z_k Z_l e^2}{|\mathbf{r}-\mathbf{r}'|} e^{-|\mathbf{r}-\mathbf{r}'|/\lambda}, \tag{17}$$

where $\lambda$ is the electronic screening length, the form of which is application dependent [36]. Here, we will employ the Debye-Hückel screening length, as described below. Because of the special nature of electron dynamics and our assumption in (16), we will abbreviate our notation such that sums over all species will henceforth refer only to ion species, with electrons handled separately. Then, we can write

$$\nabla_{\mathbf{r}} \sum_l \left( \int U_{kl}(\mathbf{r},\mathbf{r}') n_l(\mathbf{r}',t)\, \mathrm{d}\mathbf{r}' \right) = Z_k e \nabla_{\mathbf{r}} \phi(\mathbf{r},t), \tag{18}$$

where the electrostatic potential $\phi$ is

$$\phi(\mathbf{r},t) = \int \rho(\mathbf{r}',t) \left( \frac{e^{-|\mathbf{r}-\mathbf{r}'|/\lambda}}{|\mathbf{r}-\mathbf{r}'|} \right) \mathrm{d}\mathbf{r}', \tag{19}$$

and the total charge density $\rho$ is given by

$$\rho(\mathbf{r},t) = -en_e^0 + \sum_l Z_l e n_l(\mathbf{r},t). \tag{20}$$

Here, the contribution of the background electron density $n_e^0$ to $\rho$ shifts the charge density by a constant amount, and the contribution of the linear screening electron clouds $\Delta n_e(\mathbf{r})$ is modeled by the Yukawa potential in (20).

For three-dimensional Yukawa systems, this electric potential can also be computed by solving the screened Poisson equation:

$$-\nabla_{\mathbf{r}}^2 \phi + \frac{1}{\lambda^2}\phi = 4\pi\rho(\mathbf{r},t). \tag{21}$$

This arises from the fact that the Green's function solution for (21) can be expressed as (19). We can now write the full partial differential kinetic equation for $f_k$ as

$$\frac{\partial f_k}{\partial t} + \mathbf{v}\cdot\nabla_{\mathbf{r}} f_k - \frac{Z_k e}{m_k} \nabla_{\mathbf{r}}\phi \cdot \nabla_{\mathbf{v}} f_k = \sum_l C'_{kl}. \tag{22}$$

This kinetic equation defines our macroscale model, save for the collision terms $C'_{kl}$.

Different approximations for the functional form of $C'_{kl}$, and thus $f_{kl}$, yield different kinetic models. In this work, we choose the Bhatnagar-Gross-Krook (BGK) model because it requires only microscale data in the form of scalar relaxation times, rather than higher-dimensional cross-section data. To define the BGK model, we take

$$C'_{kl} \approx \frac{f_{kl}^{eq}(\mathbf{r},\mathbf{v},t) - f_k(\mathbf{r},\mathbf{v},t)}{\tau_{kl}}, \tag{23}$$

where $\tau_{kl}$ is a relaxation parameter, and the indices $k$ and $l$ denote species pairs, including self-pairs. The target distributions $f_{kl}^{eq}$ are Maxwellian, with bulk velocity $\mathbf{u}_{kl}$ and temperature $T_{kl}$:

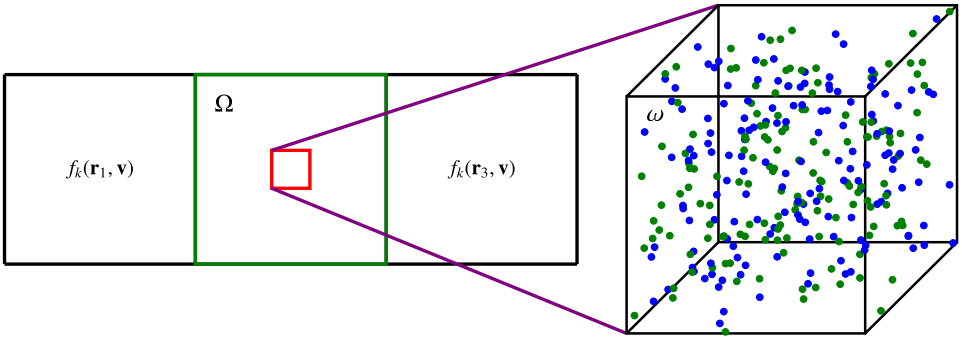


**Fig. 1.** A sketch of an MD simulation on a domain $\omega$ embedded within a spatial region $\Omega$. The ions in $\omega$ are initialized with distributions $f_k(\mathbf{r}_2, \mathbf{v})$. The resultant trajectories inform the relaxation rates employed in $\Omega$ at future kinetic timesteps.

$$f_{kl}^{eq} = n_k \exp\left(-\frac{m_k|\mathbf{v}-\mathbf{u}_{kl}|^2}{2T_{kl}}\right). \tag{24}$$

where, for species with bulk velocities $\mathbf{u}_k$ and $\mathbf{u}_l$ and temperatures $T_k$ and $T_l$ (see 4.2),

$$\mathbf{u}_{kl} = \frac{m_k n_k \tau_{lk}\mathbf{u}_k + m_l n_l \tau_{kl}\mathbf{u}_l}{m_k n_k \tau_{lk} + m_l n_l \tau_{kl}}, \tag{25}$$

$$T_{kl} = \frac{n_k \tau_{lk}\mathbf{u}_k + n_l \tau_{kl}\mathbf{u}_l}{n_k \tau_{lk} + n_l \tau_{kl}} + \frac{m_k n_k \tau_{lk}(u_k^2 - u_{kl}^2) + m_l n_l \tau_{kl}(u_l^2 - u_{kl}^2)}{3(n_k \tau_{lk} + n_l \tau_{kl})}. \tag{26}$$

The mixture quantities $\mathbf{u}_{kl}$ and $T_{kl}$ depend on the collision rates $\tau_{kl}$ and $\tau_{lk}$ and are defined such that the collisional model conserves mass, momentum, and energy and satisfies Boltzmann's H-Theorem; see [2] for more detail. Standard formulas for relaxation times for plasmas rely on a series of approximations that are only appropriate in a narrow range of parameter space [37,38]. These are phenomenological quantities that can only be computed explicitly under specific conditions and assumptions, and many physically relevant scenarios that may be encountered during a simulation, such as moderate coupling and distributions too far out of equilibrium, violate the assumptions used to derive the standard formulas. Furthermore, because the relaxation times depend on a very high-dimensional parameter space, namely, the parameter space of possible distributions, we cannot realistically predict these scenarios *a priori* by precomputing the relaxation times in a manner equivalent to generating an equation-of-state table.

In summary, we have derived VBGK,

$$\begin{aligned} &\frac{\partial f_k}{\partial t} + \mathbf{v}\cdot\nabla_{\mathbf{r}} f_k - \frac{Z_k e}{m_k}\nabla_{\mathbf{r}}\phi\cdot\nabla_{\mathbf{v}} f_k = \sum_l \frac{f_{kl}^{eq} - f_k}{\tau_{kl}} \\ &-\nabla_{\mathbf{r}}^2\phi + \frac{1}{\lambda^2}\phi = 4\pi\left(\sum_k Z_k e n_k - e n_e^0\right) \end{aligned} \tag{27}$$

directly from the microscopic variables evolved with MD. The VGBK system is closed when the $\tau_{kl}$ are specified; here, they are obtained from a microscale model.

## 3. Implementation of the multiscale model

The BGK approximation greatly simplifies the closure data transfer in this HMM scheme by encoding collisional details into a single relaxation rate $\tau_{kl}$ per species pair. We compute $\tau_{kl}$ *in situ* using embedded MD simulations under the HMM framework. This computation requires that characteristic spatial and temporal scales of the MD system be much smaller than those in the macroscopic system and that the information used at the two scales be consistent.

To estimate $\tau_{kl}$ for a region $\Omega$ with known distributions $f_k(\mathbf{r}, \mathbf{v})$ in the region, we define a small subdomain $\omega$ embedded in $\Omega$ and assume that the distributions $f_k$ are constant in this subdomain; see Fig. 1. We then initialize the MD ions in $\omega$ from these distributions and perform MD simulations to determine the relaxation rates.

### 3.1. Initializing MD simulations from kinetic data

Upon initial placement of the ions in the MD domain, interparticle correlations will not be consistent with the desired state. As the initial particle correlations develop, an exchange between potential energy and kinetic energy [39] will heat the system away from the desired $f_k$. Thermostats [40,41] are used to equilibrate the system to the desired initial thermodynamic state with consistent microscopic spatial ordering [42].

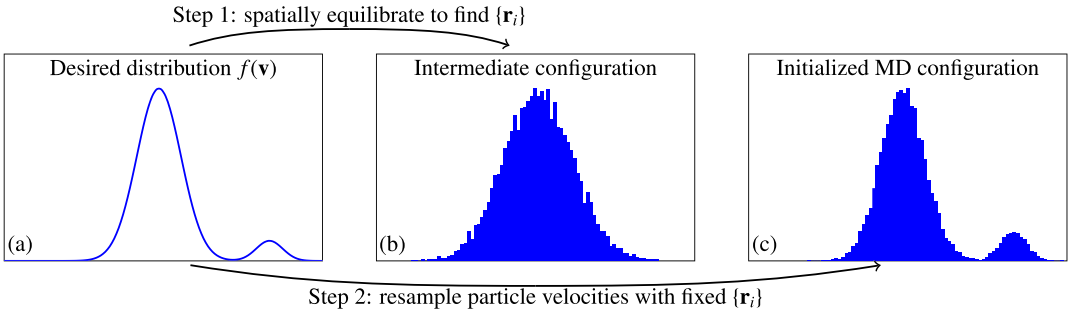


**Fig. 2.** The process of initializing an MD simulation to a desired nonequilibrium distribution. **(a)** We start with a potentially nonequilibrium distribution $f(\mathbf{v})$. **(b)** The MD particles are driven by a Langevin thermostat to a Maxwellian distribution $f_{dM}(\mathbf{v}; n, \mathbf{u}, \mathbf{T})$, such that the zeroth through second moments match the desired distribution, and interparticle correlations are consistent with the equilibrium distribution. **(c)** The particle velocities $\{\mathbf{v}_i\}$ are resampled directly from the desired distribution, while keeping the particle positions $\{\mathbf{r}_i\}$ fixed to maintain reasonable interparticle correlations. If multiple species are present, these steps are performed simultaneously for all species in the cell so that the initial MD condition is consistent with the multispecies distribution.

A difficulty that arises when initializing MD in the HMM framework presented in this paper is that the kinetic distributions $f_k$ are potentially nonequilibrium distributions, whereas most tools (e.g., thermostats) for initializing MD rely on near-equilibrium assumptions. We first construct the drifting Maxwellians $f_{k,dM}(\mathbf{v}; n_k, \mathbf{u}_k, \mathbf{T}_k)$, where $n_k$, $\mathbf{u}_k$, and $\mathbf{T}_k$ are defined to match the density, momentum, and kinetic temperature of the nonequilibrium kinetic distributions $f_k$ (for more details, see (36)-(38)). We then instantiate an MD system and, using a stochastic thermostat based on Langevin dynamics, drive each species in the NVT ensemble towards the corresponding $f_{k,dM}$. This initialization ensures that reasonable interparticle correlations, consistent with the zeroth through second moments of the distribution function, are achieved.

After the equilibration phase, we compute and numerically invert the cumulative distribution function corresponding to each $f_k(\mathbf{v})$. We then reassign the particle velocities so that the MD particle velocities match the potentially non-equilibrium kinetic state of the distribution functions by drawing samples from the uniform distribution and computing the corresponding velocity from the inverted cumulative distributions. Once the resampling procedure is completed, we consider the MD system to be initialized and can compute the desired microscopic data by propagating the system in the NVE ensemble. This procedure is illustrated for a bump-on-tail example in Fig. 2.

It is important to note that by resampling the velocities, we lose the particle correlations that depend on both positions *and* velocities. These correlations are a casualty of the multiscale method; the macroscale model contains insufficient information to fully and self-consistently specify the microscale. However, we have found that in practice these lost correlations did not have a statistically significant effect on the evolution of systems where $f_k(\mathbf{v})$ are equilibrium distributions or nonequilibrium distributions that can be represented as a superposition of Maxwellians (e.g. bump on tail). A more thorough exploration of this issue in the context of nonequilibrium distributions will be a subject for future work.

### 3.2. Calculating collision rates from MD data

The relaxation rates $\tau_{kl}$ must be extracted from some statistical observable in the MD system. The relaxation rates describe the rates of change of the distribution functions due to the kinetic system being out of equilibrium, so we compute $\tau_{kl}$ by ensuring that the rate of change of some quantity is the same for both the kinetic and MD systems. The mean-field electric field is not well-defined in MD, so this quantity must isolate "collisions" from the mean-field, an artificial separation in an MD context.

Because the mean-field cannot change the entropy, the evolution of the Boltzmann $H$ function isolates the effect of collisions. The $H_k$ function for each species $k$ is defined as

$$H_k(\mathbf{r}, t) = \int f_k(\mathbf{r}, \mathbf{v}, t) \log(f_k(\mathbf{r}, \mathbf{v}, t))\, \mathrm{d}\mathbf{v}. \tag{28}$$

Integrating the $H_k$ function for each species over the domain and summing over species yields the negative entropy of the system. The total $H$ in a system is a decreasing function of time and is constant only when the system is in global equilibrium.

Although the total $H$ decreases monotonically, $H_k$ for each individual species may increase because of interactions with other species. We compute $\tau_{kl}$ by matching the MD and kinetic interpretations of the rate of change of $H_k$ for each species at each position, due specifically to collisional interactions, including self-collisions. This guarantees that we compute $\tau_{kl}$ by forcing a fundamental, collision-dependent physical quantity to change in the kinetic model in accordance with the more detailed molecular model.

The rate of change of $H_k$ according to the kinetic model, when disregarding advection, is

$$\frac{dH_k^{KT}}{dt} = \sum_l \frac{1}{\tau_{kl}(\mathbf{r})} \int (f_{kl}^{eq} - f_k) \log(f_k)\, \mathrm{d}\mathbf{v}. \tag{29}$$

The right-hand-side of (29) depends *only* on the collisional terms in the Vlasov-BGK equation (see C.2 for a more detailed derivation), allowing us to isolate the terms involving $\tau_{kl}$. The equivalent rate of change in a molecular model is

$$\frac{dH_k^{MD}}{dt} = \sum_l \left\langle \sum_{\substack{i\in S_k \\ j\in S_l}} \frac{\mathbf{F}_{ij}}{m_k} \cdot \nabla_{\mathbf{v}} \left(\log(f_k)\right)|_{\mathbf{v}=\mathbf{v}_i} \right\rangle, \tag{30}$$

where $S_k$ is the set of indices corresponding to ions of species $k$, and $\mathbf{F}_{ij}$ is the force exerted on particle $i$ by particle $j$. The MD data are computed as time-averaged quantities, assuming ergodicity and that the kinetic variables do not change significantly over the course of a microscale simulation. This latter requirement limits the amount of time over which we can average the data. The resulting data is subject to statistical noise because of finite particle number and variation in the initialization. The former can be mitigated by using a larger number of particles, and the latter by aggregating data from several independent MD simulations run in parallel. Because the MD simulation domain is much smaller than the kinetic finite-volume cell, the quantities gathered using MD must be scaled up by the volume differential.

Noting that both (29) and (30) are expressed as sums over all species, we can isolate interactions between species pairs by equating the two expressions term-wise to specifically match the entropy change of species $k$ due to interactions with any species $l$:

$$\frac{1}{\tau_{kl}} \int (f_{kl}^{eq} - f_k) \log(f_k)\, \mathrm{d}\mathbf{v} = \frac{V_{KT}}{V_{MD}} \sum_{\substack{i\in S_k \\ j\in S_l}} \frac{\mathbf{F}_{ij}}{m_k} \cdot \sum_{i\in S_k} \nabla_{\mathbf{v}} (\log(f_k))|_{\mathbf{v}=\mathbf{v}_i}. \tag{31}$$

This equation can be solved directly when $k = l$, as $f_{kk}^{eq}$ does not depend on $\tau_{kk}$. However, $f_{kl}^{eq}$ and $f_{lk}^{eq}$ are nonlinear functions of the ratio $\tau_{kl}/\tau_{lk}$ (see (25), (26)), resulting in a pair of coupled nonlinear equations for each $k \neq l$ pair. When both species are near equilibrium, the system of equations becomes ill-conditioned. To account for statistical noise in the MD computation of $dH_k^{MD}/dt$ and to avoid a potential singularity, when $k \neq l$ we solve the coupled equations for $\tau_{kl}$ in (31) by minimizing the error in the least-squares sense.

Given a choice of $\tau_{kl}/\tau_{lk}$, there is a *linear* least-squares solution, but ambiguity remains in the choice of this ratio. Two possible constraints are $n_k\tau_{lk} = n_l\tau_{kl}$ or $m_k n_k \tau_{lk} = m_l n_l \tau_{kl}$, which arise as a consequence of deriving a BGK model that matches, respectively, energy or momentum exchange rates with the Boltzmann model under some assumptions [2]. An alternative that empirically tends to yield better agreement between BGK and MD systems is to leave $\tau_{kl}/\tau_{lk}$ as a free parameter and use a *nonlinear* least squares optimization procedure to choose the ratio of relaxation rates that best matches $dH/dt$ between the macroscopic and microscopic scales. These approaches to defining the collision ratios will be examined in the numerical results below.

### 3.3. Quantifying when to call the microscopic model

The HMM model is evolved by alternating between the kinetic model to evolve the macroscopic system and the MD model to compute collision rates. It remains to be specified when the kinetic model should interrogate the MD to update the collision rates as conditions change. We choose to measure the relative change in distributions $f_k(\mathbf{r}, \mathbf{v})$ from some initial state

$$E_k(\mathbf{r}) = \frac{\| f_k(\mathbf{r}, t) - f_k(\mathbf{r}, t_0)\|_2}{\| f_k(\mathbf{r}, t_0)\|_2}, \tag{32}$$

where $t_0$ is a reference time. When this ratio increases beyond a user-defined threshold, the kinetic model pauses and requests new collision times from the MD data based on the current distribution functions $f_k$. The reference time $t_0$ is reset to the current time, and the kinetic calculation continues with the new collision times. In our simulations, we found that $E_k > 0.1$ was a reasonable value for refreshing the collision rates.

### 3.4. Algorithm

The HMM described in this paper can be summarized as follows:

1. Given the initial macroscopic state in each kinetic simulation cell, run a small MD simulation to compute initial values for each collision time $\tau_{kl}(\mathbf{r})$.
2. Evolve the kinetic equation in each cell using the computed $\tau_{kl}(\mathbf{r})$.
3. Calculate the metric $E_k(\mathbf{r})$ in (32), and compute new collision times $\tau_{kl}(\mathbf{r})$ if a distribution has significantly changed.
4. Repeat steps 2 and 3 until the end time of the simulation is reached.

The resulting simulation, while bottlenecked by MD simulations, is able to probe much larger systems for a much longer time than a full MD simulation. Furthermore, the relaxation times used in the Vlasov-BGK equation will cause the kinetic

system to accurately track the entropy changes implied by the MD description. This results in a model far more accurate and flexible than any current Vlasov-BGK model.

## 4. Numerical results

In this paper, we present proof-of-concept multispecies kinetic problems with initial conditions far from equilibrium. Given that the collision rates are local quantities, we choose 0D-3V (zero dimension in physical space, three dimensions in velocity space) test cases for which we can compute full MD reference solutions at reasonable computational cost. The ability to perform complete microscopic simulations allows us to probe the advantages and limitations of the multiscale framework by comparing to a ground truth. Future work will extend this model to a more realistic 1D-3V case, such as interface evolution in ICF.

The problems we selected are in the weak to moderate coupling regime, where neither the MD nor the VBGK models by themselves are optimal. Assuming a Yukawa potential, the coupling parameter $\Gamma_k = Z_k^2 e^2/(a_k T_k) e^{-a_k/\lambda}$ describes the ratio of potential energy to kinetic energy for a given species, where $a_k = (3/(4\pi n_k))^{1/3}$ is the interatomic spacing of species $k$; note that this definition differs from the more common bare coupling parameter $\Gamma_k^{(b)} = Z_k^2 e^2/(a_k T_k)$ to include a reduction in the potential energy due to screening. The transition regime of interest, where collisions are non-negligible but also insufficiently frequent to rapidly drive distributions to equilibrium, corresponds to roughly $\Gamma \sim O(0.1 - 1)$.

### 4.1. Molecular dynamics implementation

Given an initial configuration $\left(\{\mathbf{r}_i(0)\}_{i=1}^N, \{\mathbf{v}_i(0)\}_{i=1}^N\right)$, the MD simulation evolves in the NVE ensemble according to

$$\begin{aligned}
\dot{\mathbf{r}}_i &= \frac{1}{m_i} \nabla_{\mathbf{v}_i}(H) = \mathbf{v}_i, \\
\dot{\mathbf{v}}_i &= -\frac{1}{m_i} \nabla_{\mathbf{r}_i}(H) = \frac{1}{m_i} \mathbf{F}_i(\mathbf{r}_1, \ldots, \mathbf{r}_N), \\
\mathbf{F}_i &= -\sum_{j \neq i} \nabla_{\mathbf{r}_i}(U_{ij}(\mathbf{r}_i, \mathbf{r}_j)),
\end{aligned} \tag{33}$$

where $\mathbf{F}_i$ is the force exerted on ion $i$ due to all other ions. To compute the screening length, we assume a fixed electron temperature corresponding to the initial density-weighted mixture temperature and use the Debye length as the characteristic length:

$$\lambda = \lambda_D = \sqrt{\frac{T_e}{4\pi n_e e^2}}, \tag{34}$$

$$n_e = \sum_k Z_k n_k. \tag{35}$$

The equations of motion are integrated using a parallelized velocity Verlet integrator using a nearest-neighbor list to achieve $\mathcal{O}(N)$ scaling. A reversible multiple time-step method [43] is used to handle hard collisions, based on observed jumps in the total energy. Equilibration to the desired initial distributions is achieved by driving the system in the NVT ensemble using a Langevin thermostat. The thermostat is not active during the observational phase.

For all test cases presented, we chose the MD timestep such that energy fluctuations and drift due to numerical effects remained below $10^{-4}$, ensuring the results are converged with respect to the timestep. We chose the domain size such that the number of particles was sufficient to compute the desired statistics. All computed macroscopic properties are averaged over multiple plasma periods to ensure that short-term fluctuations do not pollute the outputs.

### 4.2. BGK implementation

The 0D-3V Vlasov-BGK equation (27) is evolved in time with a second-order SSP Runge-Kutta method [44]. For each species, we make a uniform discretization of velocity space, with the maximum velocity chosen to be a multiple of the maximum expected thermal velocity for that species in the simulation. Note that because each species has a separate velocity grid, the BGK model is not constrained by the mass ratio of the species when defining the velocity grids, which is a source of great expense in discrete velocity implementations of e.g. Boltzmann or Fokker-Planck kinetic models.

To compute the macroscopic observables, which are parameters of the Maxwellians in the BGK operators, we compute the moments,

$$n_k(\mathbf{r}, t) = \int f_k(\mathbf{r}, \mathbf{v}, t)\, \mathrm{d}\mathbf{v}, \tag{36}$$

**Table 1**
Number density, initial temperature, charge, and coupling for the temperature relaxation test case.

| | $n$ (1/cc) | $T_0$ (eV) | $Z$ | $\Gamma$ |
|---|---|---|---|---|
| Hydrogen | $6.0 \cdot 10^{22}$ | 1000 | 1.0 | $9.1 \cdot 10^{-3}$ |
| Aluminum | $6.0 \cdot 10^{22}$ | 500 | 11.5 | 2.4 |

**Table 2**
Domain size, time step, final temperature, and run time for the MD, VBGK, and HMM hybrid models. Run time refers to the wall time on 12 cores with OpenMP parallelism, including averaging over 5 runs for the full MD simulation.

| | $L/\lambda_D$ | $\Delta t_{MD}$ (s) | $\Delta t_{VBGK}$ (s) | $T_{eq}$ (eV) | Run time (hrs) |
|---|---|---|---|---|---|
| MD | 21 | $1.46 \cdot 10^{-18}$ | N/A | 738 | 1800 |
| VBGK (SM rates) | N/A | N/A | $1.0 \cdot 10^{-15}$ | 750 | 2 |
| MD-VBGK HMM | 18 | $4.38 \cdot 10^{-18}$ | $1.0 \cdot 10^{-15}$ | 750 | 18 |

$$\mathbf{u}_k(\mathbf{r}, t) = \frac{1}{n_k} \int \mathbf{v} f_k(\mathbf{r}, \mathbf{v}, t) \, \mathrm{d}\mathbf{v}, \tag{37}$$

$$\mathbf{T}_k(\mathbf{r}, t) = \frac{m_k}{3n_k} \int (\mathbf{v} - \mathbf{u}_k(\mathbf{r}, t)) (\mathbf{v} - \mathbf{u}_k(\mathbf{r}, t))^T f_k(\mathbf{r}, \mathbf{v}, t) \, \mathrm{d}\mathbf{v}, \tag{38}$$

using a numerical quadrature. Here, the kinetic temperature for a potentially non-equilibrium distribution is defined as $T_k = \mathrm{Tr}(\mathbf{T}_k)$. For inter-species interactions, these moments are used to form the mixture moments $\mathbf{u}_{ij}$ and $T_{ij}$ (25), (26). The collision times $\tau_{kl}$ are provided by the MD through the HMM framework.

Depending on the symmetries of the problem, we may be interested in higher moments, such as the vector heat flux and kurtosis

$$\mathbf{q}_k = \frac{m_k}{2} \int (\mathbf{v} - \mathbf{u}_k(\mathbf{r}, t)) |\mathbf{v} - \mathbf{u}_k(\mathbf{r}, t)|^2 f_k(\mathbf{r}, \mathbf{v}, t) \, \mathrm{d}\mathbf{v}, \tag{39}$$

$$\mathcal{K}_k = \frac{m_k^2}{n_k T_k^2} \int |\mathbf{v} - \mathbf{u}_k(\mathbf{r}, t)|^4 f_k(\mathbf{r}, \mathbf{v}, t) \, \mathrm{d}\mathbf{v}, \tag{40}$$

which provide further information about the shape of a distribution. For reference, for a Maxwellian in a 3D velocity space these values are $\mathbf{q} = 0$ and $\mathcal{K} = 15$.

For further details on the implementation, see [2].

### 4.3. Temperature-relaxation test case

First, we apply our approach to a two-species, 0D temperature-relaxation problem. The system initially comprises Maxwellian-distributed aluminum and hydrogen ions with zero bulk velocity at equal density, corresponding approximately to solid-density aluminum. The MD simulation employs periodic boundary conditions. Over time, the system relaxes to a thermal equilibrium. For comparisons, we performed five full MD simulations (averaged to approximate an ensemble average) and one standard BGK simulation, using theoretical values for $\tau_{kl}$ specific to temperature-relaxation problems [2].

The initial conditions and simulation parameters are listed in Tables 1 and 2. The stringent time-step requirement for the MD simulations is driven by energy-conservation requirements, as the kinetic hydrogen ions otherwise experience hard collisions with the highly charged aluminum, causing nonphysical increases in the energy. The time step can be increased significantly for the HMM simulation. We also decreased the domain size for MD queries by the HMM simulation compared to the full MD, which reduced the number of particles and further decreased computational cost.

The data used to update relaxation rates was averaged over three independently initiated and equilibrated MD runs. The initialization and equilibration contributes to a large portion of the computational time of the HMM but is necessary to maintain stochasticity of the MD simulations. The relaxation rates were updated whenever the error metric in (32) reached 10%.

Fig. 3 shows the evolution of the system using the MD, VBGK, and BGK-MD HMM approaches. We find that the SM cross-sections underestimate the relaxation time by about a factor of three. This is not unexpected, as these collision rates are constructed to match quantities from Boltzmann for perturbed Maxwellians, while this test case has a large difference in temperatures. In contrast, the BGK-MD HMM approach computes larger relaxation times than the naive VBGK model, and underestimates the overall relaxation time by only a factor of two. Moreover, the HMM formulation captures the behavior of the hydrogen fairly well at early times, and the main discrepancy from the full MD is in the behavior of the aluminum. The difference in aluminum evolution between the two models occurs because the moderately coupled aluminum ions have higher potential energy in the equilibrium state than at the initial condition. Consequently, kinetic energy is converted to potential energy as the system evolves, resulting in a lower final temperature than what is predicted when assuming

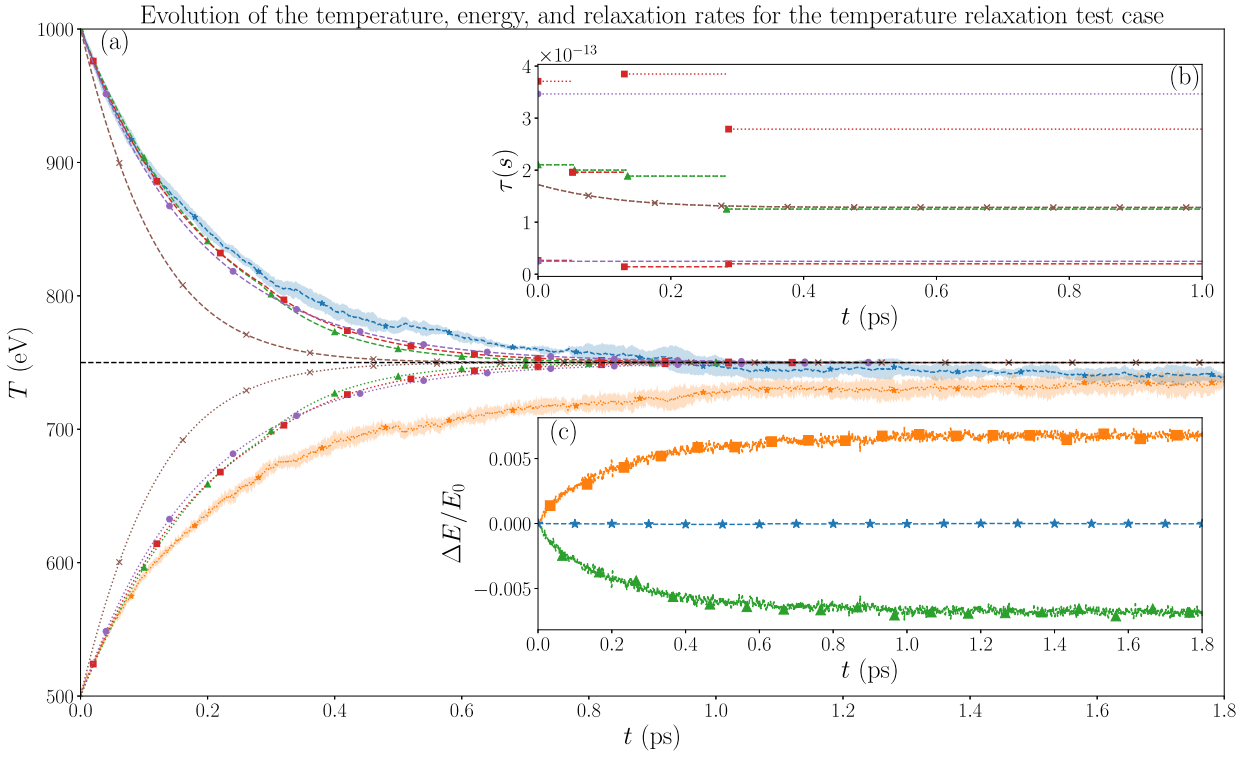


**Fig. 3.** **(a)** The time evolution of the temperature is shown. We show results for hydrogen and aluminum in dashed and dotted lines, respectively. Full MD results for hydrogen (blue stars) and aluminum (orange stars) are shown with a 1-$\sigma$ error band (shaded). The HMM cases shown include simulations performed using the rate-update procedure with temperature (green triangles) and optimized (red squares) relaxation rates, and using constant relaxation rates calculated using the optimization procedure at the initial condition (purple circles). VBGK results with SM cross-sections assuming temperature relaxation are also shown (brown "x"es). The dashed black line shows the 750 eV equilibrium temperature, assuming kinetic energy conservation. **(b)** Relaxation rates for the HMM and VBGK cases are shown. Both $\tau_{H,Al}$ (dashed lines) and $\tau_{Al,H}$ (dotted lines) are shown; note that under the temperature relaxation assumption, these rates are equal. **(c)** Changes in the total (blue stars), kinetic (orange squares), and potential (green triangles) energy, normalized by the initial total energy for the full MD simulation, are shown.

conservation of kinetic energy alone. The pull towards a higher potential-energy surface also greatly increases the relaxation time of the aluminum species. Because the VBGK system conserves *kinetic energy* and has no notion of the potential energy, it is unable to capture this effect.

For this relatively simple problem, individual species stay nearly Maxwellian throughout, and we find that the choice of relaxation-rate ratio $\tau_{H,Al}/\tau_{Al,H}$ has only a small effect. However, when using the optimization procedure to compute relaxation rates, evolution matches the full MD slightly more closely than when using temperature relaxation rates ($n_k\tau_{lk} = n_l\tau_{kl}$). We also find that using a constant relaxation rate computed using our method at the initial conditions performs nearly as well as using a relaxation rate that is updated throughout the simulations. The effects of updating the relaxation rate are minimal because most of the relaxation occurs early in the simulation and the initial relaxation rates have outsize effect on the evolution of the system towards equilibrium. Future studies on 1D systems will help to illuminate the effects of the frequency with which the relaxation rates are updated.

### *4.4. Momentum-relaxation test case*

Next, we conduct a simulation of a 0D, two-species, same-temperature momentum-relaxation problem. In this case, hydrogen and helium ions are initially at the same density and temperature, but the hydrogen ions initially have a bulk velocity equal to their thermal speed. The two species relax towards a configuration in thermal and momentum equilibrium. This HMM simulation is compared with a reference MD simulation (averaging over five runs) and a naive VBGK simulation, with theoretical temperature and momentum relaxation rates [2]. The initial conditions and parameters of the simulation are given in Tables 3 and 4, and the resulting equilibration and relaxation rates are shown in Fig. 4.

Although the speedup is less dramatic for this problem compared with the temperature relaxation case, the benefit of the multiscale model over the naive VBGK model is even clearer. Whereas the relaxation times derived from the SM theory underestimate the equilibration time by approximately a factor of ten, the HMM simulations result in a relaxation time comparable to that observed in the full MD simulations. Moreover, because the momentum relaxation problem is less strongly coupled, we do not see the energy exchange effects observed in the temperature-relaxation problem, and the kinetic energy conservation assumption of the VBGK is not violated.

**Table 3**
Number density, initial temperature and velocity, charge, and coupling for the momentum relaxation case.

| | $n$ (1/cc) | $T_0$ (eV) | $u_0/v_{th0,H}$ | $Z$ | $\Gamma$ |
|---|---|---|---|---|---|
| Hydrogen | $6.0 \cdot 10^{22}$ | 250 | 1.0 | 1.0 | $3.6 \cdot 10^{-2}$ |
| Helium | $6.0 \cdot 10^{22}$ | 250 | 0 | 2.0 | 0.15 |

**Table 4**
Simulation parameters used for the momentum-relaxation case performed using the MD, VBGK, and HMM hybrid formulations. Run time refers to the total wall time on 12 cores with OpenMP parallelism and includes averaging over 5 runs for the full MD simulation.

| | $L/\lambda_D$ | $\Delta t_{MD}$ (s) | $\Delta t_{VBGK}$ (s) | Run time (hrs) |
|---|---|---|---|---|
| MD | 18 | $3.25 \cdot 10^{-18}$ | N/A | 510 |
| VBGK (SM rates) | N/A | N/A | $1.0 \cdot 10^{-16}$ | 1.5 |
| MD-VBGK HMM | 18 | $9.74 \cdot 10^{-18}$ | $1.0 \cdot 10^{-15}$ | 37 |

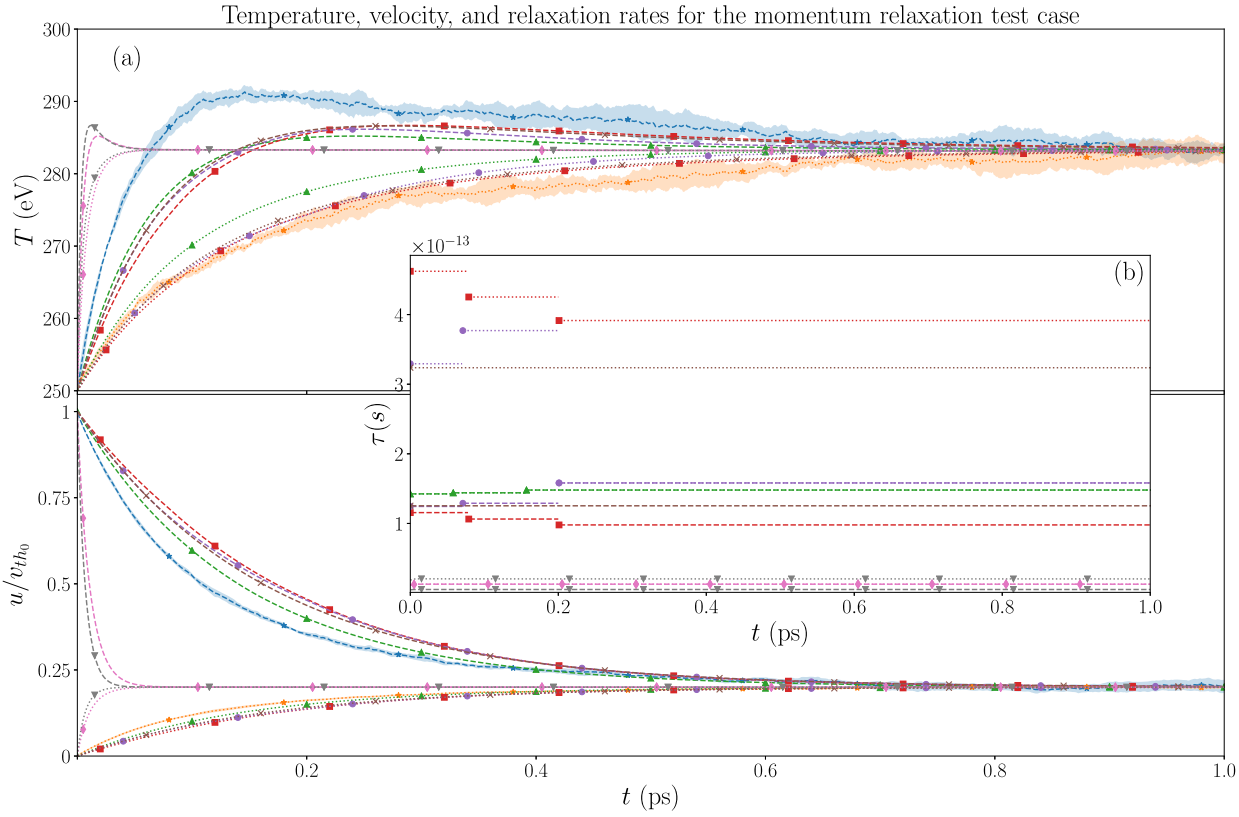


**Fig. 4.** **(a)** The time evolution of the temperature and velocity, normalized by initial hydrogen thermal speed, are shown. Hydrogen and helium are shown in dashed and dotted lines, respectively. Full MD time histories of the hydrogen (blue stars) and helium (orange stars) include 1-$\sigma$ error bands (shaded). The HMM cases shown include simulations using the rate-update procedure with temperature (green upward triangles), momentum (red squares), and optimized (purple circles) relaxation rates, and using constant relaxation rates obtained using the optimization procedure at the initial condition (brown "x" crosses). VBGK results with SM cross-sections obtained using temperature (pink diamonds) and momentum (grey downward triangles) relaxation rates are also shown. **(b)** Relaxation rates for the HMM and VBGK cases are shown. Both $\tau_{H,He}$ (dashed lines) and $\tau_{He,H}$ (dotted lines) are shown. Note that under the temperature-relaxation assumption, these rates are equal.

Because our optimization procedure acts on entropy generation, rather than the individual temperature or momentum relaxations, we expect the relaxation of the distributions towards equilibrium to be captured to the best extent possible given the assumptions inherent in the BGK relaxation model. Curiously, the HMM model based on a momentum relation ($m_H n_H \tau_{He,H} = m_{He} n_{He} \tau_{H,He}$) appears to best capture the relaxation in temperature, whereas the HMM model based on a temperature relation ($n_H \tau_{He,H} = n_{He} \tau_{H,He}$) best captures the momentum relaxation behavior. Although all choices explored in the ratio $\tau_{H,He}/\tau_{He,H}$ capture the overall relaxation time fairly well, no choice fully captures the temperature or momen-

**Table 5**
Initial number density, bulk velocity, pressure tensor components, and coupling for the BoT test case.

| $n_0$ (1/cc) | $n_1$ | $T_0$ (eV) | $T_1$ (eV) | $u_0$ | $u_1$ (eV) | $\Gamma$ |
|---|---|---|---|---|---|---|
| $4.8 \cdot 10^{22}$ | $1.2 \cdot 10^{22}$ | 100 | 25 | 0 | $3v_{th_0}$ | $3.6 \cdot 10^{-2}$ |

**Table 6**
Domain size, time step, and run time for the single-species BoT case performed using the MD, VBGK, and HMM hybrid formulations. Run time refers to the total wall time on 12 cores with OpenMP parallelism and includes averaging over 5 runs for the full MD simulation.

| | $L/\lambda_D$ | $\Delta t_{MD}$ (s) | $\Delta t_{VBGK}$ (s) | Run time (hrs) |
|---|---|---|---|---|
| MD | 18 | $3.63 \cdot 10^{-18}$ | N/A | 1220 |
| VBGK (SM rates) | N/A | N/A | $1.0 \cdot 10^{-15}$ | 1.1 |
| MD-VBGK HMM | 18 | $1.09 \cdot 10^{-17}$ | $1.0 \cdot 10^{-15}$ | 73 |

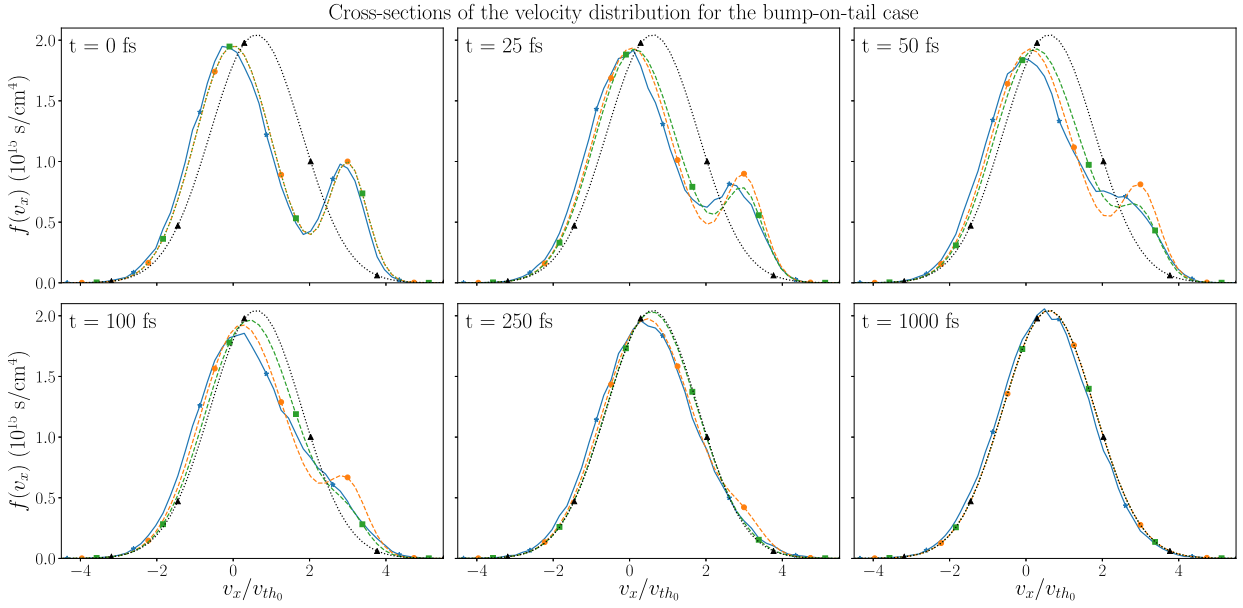


**Fig. 5.** Time snapshots of the velocity distribution with $y$- and $z$-dependence integrated out, for the full MD (solid blue, stars), VBGK using SM cross-sections (dashed green, squares), and HMM (dotted orange, circles) simulations. Velocities are normalized by the initial thermal speed of the bulk component $v_{th0}$. Note the final conditions for the VBGK and HMM match the equilibrium solution derived from momentum and kinetic energy conservation (dotted black, triangles).

tum evolution at early time, when the system is furthest out of equilibrium, suggesting that the underlying phenomenon cannot be captured by a single set of velocity-independent relaxation rates.

The multispecies temperature- and momentum-relaxation test cases primarily test the ability of our method to capture the interspecies relaxation term, although some non-equilibrium self-relaxation occurs in the momentum-relaxation case due to the collisionally damped two-stream instability.

### *4.5. Bump-on-tail test case*

Our final test case focuses on single-species relaxation for a bump-on-tail (BoT) initial condition, which models a population of hydrogen ions streaming into a stationary, Maxwellian hydrogen plasma. The system is initialized as a superposition of two distributions, a bulk (subscript 0) and a tail (subscript 1) distribution, such that the total ion density is $6.0 \cdot 10^{22}$ cm$^{-3}$. The bulk distribution is a 3D Maxwellian with zero velocity and temperature $T_0$. The bump distribution is initialized as a Gaussian with bulk velocity $u_1$ in the streaming direction, having a diagonal temperature tensor with $T_x = T_1/3$ and $T_y = T_z = T_0/3$.

The initialization and simulation parameters are described in Tables 5 and 6, and snapshots of the distributions as a function of the $x$-component of the velocity (with $y$- and $z$-dependence integrated out) are shown in Fig. 5. We also show time histories of the relaxation rates and higher moments of the distribution in Fig. 6. We split the contributions to

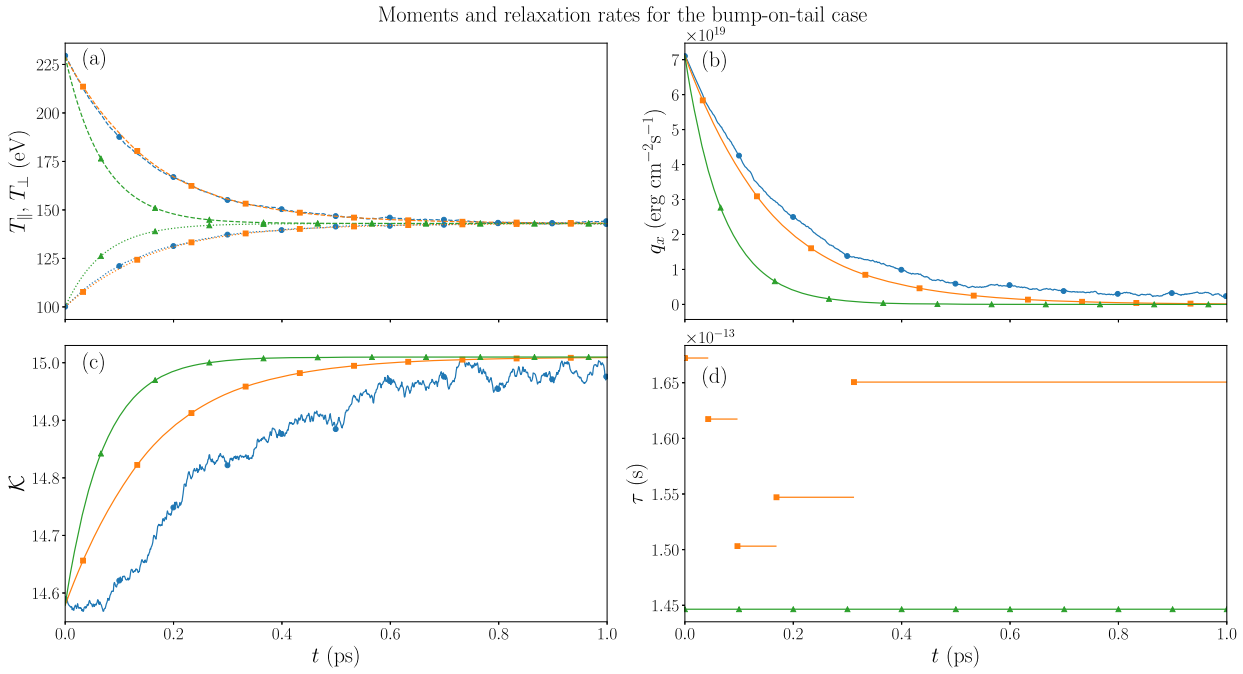


**Fig. 6.** Evolution of the moments and relaxation rates for the BoT simulations with the full MD (blue circles), VBGK with SM cross-sections (green triangles), and HMM (orange squares) formulations. **(a)** Kinetic temperature contributions from the streaming (dashed) and non-streaming (dotted) directions. **(b)** Heat flux in the streaming direction. **(c)** Kurtosis. **(d)** Self-relaxation rate for the HMM and VBGK cases.

the kinetic temperature of the overall distribution into the streaming component $T_\parallel = 3T_x$ and perpendicular component $T_\perp = 3(T_y + T_z)/2$.

Even though the system is initialized very far from equilibrium, the three methods produce less starkly disparate results than in the multispecies test cases. The SM cross-sections are well-suited for capturing self-relaxation of hydrogen ions, and in fact the relaxation rate computed with the SM cross-sections differs by only 10-15% from the rates computed using the HMM formulation. Note that the standard VBGK computes a constant in time relaxation rate because the momentum and overall kinetic temperature are constant. The HMM method appears to track the equilibration rate of the MD velocity distribution in the streaming direction slightly better than the VBGK, although the bump on the tail is more slowly damped in the HMM compared with other methods.

Because it is difficult to visualize the evolution of a 3D velocity distribution, the advantage of the HMM method over the naive VBGK becomes far more apparent when examining the moments of the distribution. The HMM captures the evolution of the streaming and perpendicular kinetic temperature components nearly perfectly when compared to the reference MD simulation. The VBGK, on the other hand, overestimates the rate of energy exchange between the streaming and perpendicular directions, resulting in the temperature tensor components relaxing to the isotropic equilibrium value too rapidly. Although the HMM does not track the higher order moments as perfectly, it captures the evolution of these moments much more closely than the naive VBGK.

As we consider distributions further from equilibrium, the assumptions inherent in the BGK approximation are violated, and higher order behaviors will play a larger role in determining the evolution of the system. However, the ability of our HMM method to capture the evolution of the higher order moments relatively well using a single, velocity-independent relaxation rate is a testament to the strength of the multiscale framework. By using closure data from the microscale, we expand the scope of problems that can be handled using the Vlasov-BGK equation farther into the non-equilibrium, moderately coupled regime.

## 5. Conclusions

We have developed an HMM that couples MD with a kinetic model for use in moderately collisional plasma environments. The macroscale model is a Vlasov-BGK model, which requires only collision times as its closure data. These data are obtained from the microscopic MD simulations through the H-theorem, which isolates the collisional portion of the force from the mean-field.

As proof of concept test cases, we chose 0D multispecies temperature and momentum relaxation problems and a single-species bump-on-tail problem. These are all problems of interest in ICF [11–17] and for which we can obtain the full MD solutions for detailed comparisons with the new HMM model.

For all three test cases, the HMM method tracked the full MD result far more closely than the VBGK with SM cross-sections. Both the theoretical and HMM relaxation rates consistently overestimated the rate of relaxation towards equilibrium when compared with the evolution of the full MD system, but the HMM formulation resulted in a much smaller discrepancy. The advantage of the HMM formulation in multispecies problems was especially stark for the momentum relaxation case, where the initial conditions were very far from equilibrium. This result has implications for modeling beams of particles, which occur in a wide variety of plasma devices, such as fast electrons ahead of shock waves. For the single species case, we were also able to far better capture the evolution of moments of the distribution, tracking the exchange of energy between the streaming and perpendicular directions nearly perfectly compared with the full MD.

The primary limitation of this multiscale method is that it cannot capture behavior that cannot be modeled in the VBGK formulation with a single, velocity-independent relaxation term per species pair, for example the exchange of potential and kinetic energy as the system evolves. However, by matching the entropy generation of the full MD system, the HMM formulation produces evolution that is optimal in some sense, given the assumptions inherent in the macroscale VBGK model. The additional degree of freedom of solving for the optimal ratio $\tau_{kl}/\tau_{lk}$ provided a slight improvement in accuracy compared with choosing the ratio based on a temperature or momentum relaxation assumption. We also defined a strategy for determining when to update the relaxation rates. Although updating the relaxation rates had limited impact for the 0D problems tested, it will be critical when applying the method to 1D problems where advection significantly changes the local conditions over time.

We found that for the test cases chosen, the HMM method resulted in a speedup of between 14 and 100 compared with the full MD simulation. The MD simulations used to update the relaxation rates accounted for the vast majority of the computational cost of the VBGK method. However, by running many MD simulations in parallel, the reduction in computational cost would be far more dramatic for 1D problems of interest, where depending on the required length and time scales, a full MD simulation may be completely intractable.

This model has several potential applications. First, accurate and efficient simulations of ICF are now in reach; this work may lead to new conclusions about the role of molecular and kinetic effects in the shocks produced by fusion reactions. Second, the ultracold neutral plasma experiments described in [45–47] provide a potential experimental validation. Constructing a database of relaxation times as functions of the input distributions and interpolating between recorded points in a manner analogous to [48] could improve the efficiency of this method further. Other machine-learning and predictive techniques that allow us to minimize the time spent in MD are also being pursued. Finally, any experiment or phenomenon of non-microscopic size involving a plasma in which microscopic effects may be important can be probed with this method.

In addition to using our HMM model for specific applications, several natural extensions of the model could be pursued. First, the model may be expanded beyond the Yukawa potential, and it could be modified to incorporate explicit electron modeling. Other effects, such as energy exchange, could be incorporated as source terms to the Vlasov equation using additional closures from the microscale. Second, other kinetic models, such as the Boltzmann equation or the BBGKY hierarchy, can be similarly coupled with MD, yielding more accurate simulations. Finally, the method could be parallelized to a greater extent and applied to even larger simulations than those described here.

Hybrid modeling methods such as the HMM have the potential to capture the best features of disparate physical models. With the HMM model developed in this work, we have gained the accuracy of molecular statistics while retaining the computational feasibility of kinetic models. The result is a large increase in the number of systems that can be simulated accurately with current computational capabilities.

## CRediT authorship contribution statement

**Gil Shohet:** Data curation, Formal analysis, Investigation, Methodology, Software, Validation, Visualization, Writing - original draft, Writing - review & editing. **Jacob Price:** Formal analysis, Investigation, Methodology, Software, Validation, Writing - original draft, Writing - review & editing. **Jeffrey Haack:** Conceptualization, Methodology, Software, Writing - original draft, Writing - review & editing. **Mathieu Marciante:** Conceptualization, Methodology, Software, Writing - review & editing. **Michael S. Murillo:** Conceptualization, Funding acquisition, Methodology, Project administration, Resources, Software, Supervision, Writing - original draft, Writing - review & editing.

## Declaration of competing interest

The authors declare that they have no known competing financial interests or personal relationships that could have appeared to influence the work reported in this paper.

## Acknowledgements

This work originated as a research project through the Los Alamos National Laboratory Computational Physics Summer School. This work was supported by the US Department of Energy through the Los Alamos National Laboratory. Los Alamos National Laboratory is operated by Triad National Security, LLC, for the National Nuclear Security Administration of The U.S. Department of Energy (Contract No. 89233218CNA000001). Work by G. Shohet was partially supported by the DOE NNSA Stewardship Science Graduate Fellowship (Grant No. DE-NA0003864). Los Alamos Report LA-UR-19-26145.

## Appendix A. Derivation of kinetic moments from molecular dynamics

The kinetic equations are derived as expected values of the MD equations. Similarly, we will define the MD equivalents of kinetic moments and the Boltzmann H-function and define their KT interpretations as the expected values of those expressions. For many terms, the result is the definition typically used in KT. However, there are some subtle differences in how kinetic and potential energy are defined that must be taken into account when coupling the two theories. Consider the full system described in MD. Let $\Omega$ represent a region of the simulation corresponding to a particular VBGK finite-volume cell, and suppose units are chosen so that the volume of that cell is 1 unit. In MD, the number density of species $k$ inside $\Omega$ is given by

$$n_k^{MD} = \sum_{\substack{i\in S_k \\ \mathbf{r}_i\in\Omega}} 1. \tag{A.1}$$

We define the KT number density as the expected value of the MD density, namely,

$$\begin{aligned} n_k^{KT} \equiv \langle n_k^{\Omega}\rangle &= \left\langle \sum_{\substack{i\in S_k \\ \mathbf{r}_i\in\Omega}} 1 \right\rangle \\ &= \int \left\langle \sum_{\substack{i\in S_k \\ \mathbf{r}_i\in\Omega}} \delta(\mathbf{r}-\mathbf{r}_i)\delta(\mathbf{v}-\mathbf{v}_i) \right\rangle \mathrm{d}\mathbf{v}\mathrm{d}\mathbf{r} \\ &= \iint_{\Omega} \left\langle \sum_{i\in S_k} \delta(\mathbf{r}-\mathbf{r}_i)\delta(\mathbf{v}-\mathbf{v}_i) \right\rangle \mathrm{d}\mathbf{v}\mathrm{d}\mathbf{r} \\ &= \iint_{\Omega} f_k \,\mathrm{d}\mathbf{v}\mathrm{d}\mathbf{r} \\ &= \int f_k \,\mathrm{d}\mathbf{v}. \end{aligned}$$

In the last step, we use the fact that the distribution is assumed to be uniform over the VBGK cell. The result is that the number density of species $k$ in terms of KT variables is consistent with the MD interpretation.

The momentum of species $k$ inside $\Omega$ for MD is given by

$$(\rho_k \mathbf{u}_k)^{MD} = \sum_{\substack{i\in S_k \\ \mathbf{r}_i\in\Omega}} m_k \mathbf{v}_i. \tag{A.2}$$

Taking the expected value and using delta functions and intra-cell uniformity as above, we define the corresponding KT momentum,

$$(\rho_k \mathbf{u}_k)^{KT} \equiv \langle (\rho_k \mathbf{u}_k)^{MD}\rangle = m_k \int \mathbf{v} f_k \,\mathrm{d}\mathbf{v}.$$

The kinetic energy of species $k$ inside $\Omega$ for MD is given by

$$K_k^{MD} = \sum_{\substack{i\in S_k \\ \mathbf{r}_i\in\Omega}} \frac{m_k|\mathbf{v}_i|^2}{2}. \tag{A.3}$$

The corresponding kinetic interpretation is again defined by taking the expected value,

$$K_k^{KT} \equiv \langle K_k^{MD}\rangle = \frac{m_k}{2}\int |\mathbf{v}|^2 f_k \,\mathrm{d}\mathbf{v}.$$

The potential energy in the full MD system is given by

$$PE = \frac{1}{2}\sum_{k,l}\sum_{\substack{i\in S_k \\ j\in S_l}} U_{kl}(\mathbf{r}_i, \mathbf{r}_j). \tag{A.4}$$

Taking the expected value, we find the KT equivalent

$$PE^{KT} \equiv \langle PE \rangle = \sum_{k,l} \frac{1}{2} \int U_{kl}(\mathbf{r}, \mathbf{r}') f_{kl} \, \mathrm{d}\mathbf{r}' \mathrm{d}\mathbf{v}' \mathrm{d}\mathbf{v} \mathrm{d}\mathbf{r}.$$

This version of the potential energy is different from the standard definition of potential energy in KT, which arises from making the mean-field approximation, $f_{kl} \approx f_k f_l$:

$$\begin{aligned} PE^{MF} &\equiv \sum_{k,l} \frac{1}{2} \int U_{kl}(\mathbf{r}, \mathbf{r}') f_k(\mathbf{r}, \mathbf{v}) f_l(\mathbf{r}', \mathbf{v}') \, d\mathbf{r}' d\mathbf{r} \, d\mathbf{v}' d\mathbf{v} \\ &= \sum_{k,l} \frac{1}{2} \int U_{kl}(\mathbf{r}, \mathbf{r}') n_k(\mathbf{r}) n_l(\mathbf{r}') \, \mathrm{d}\mathbf{r}' \mathrm{d}\mathbf{r}. \end{aligned}$$

This mean-field term appears as the acceleration term in the left-hand side of the kinetic equation (22), and the remaining difference between $PE^{MF}$ and $PE^{KT}$ corresponds to the contribution of the collisions to the potential energy. This collisional contribution $PE^{\mathrm{coll}}$ has the form

$$PE^{\mathrm{coll}} = \sum_{k,l} \frac{1}{2} \int U_{kl}(\mathbf{r}, \mathbf{r}') C_{kl} \, \mathrm{d}\mathbf{r}' \mathrm{d}\mathbf{v} \mathrm{d}\mathbf{v}' \mathrm{d}\mathbf{r},$$

where $C_{kl} = f_{kl} - f_k f_l$ is the remainder of the mean-field approximation, which is not necessarily zero. Thus, the standard definition of potential energy in kinetic equations differs from what is implied by MD, and there will be an error incurred in the potential energy, and thus total energy, defined on each scale. This error cannot be avoided, and thus, we cannot force the total energy to match between scales when initializing an MD simulation. This is true whatever collision model is applied, e.g., BGK, Boltzmann, Fokker-Planck, Lenard-Balescu, or others.

Boltzmann's $H$-function at position $\mathbf{r}$ is an inherently kinetic quantity, so we define it initially in terms of kinetic variables,

$$H_k^{KT}(\mathbf{r}) = \int f_k(\mathbf{r}, \mathbf{v}) \log(f_k(\mathbf{r}, \mathbf{v})) \, \mathrm{d}\mathbf{v}. \tag{A.5}$$

This quantity can then be expressed in terms of corresponding MD variables,

$$H_k^{MD}(\mathbf{r}) = \int \langle N_k \rangle \log(\langle N_k \rangle) \, \mathrm{d}\mathbf{v}. \tag{A.6}$$

## Appendix B. The BGK approximation and the error equation

In (23), we related the BGK approximation to the MD by setting

$$C'_{kl} \approx \frac{f_{kl}^{eq}(\mathbf{r}, \mathbf{v}, t) - f_k(\mathbf{r}, \mathbf{v}, t)}{\tau_{kl}}, \tag{B.1}$$

where $C'_{kl}$ is the integral (over $\mathbf{r}'$ and $\mathbf{v}'$) of the remainder term $C_{kl}$ after making the mean-field approximation.

We can find a full expression for the errors incurred by using the BGK approximation. Let $f_k^B$ be the solution to the Vlasov-BGK equation with optimal choices for $\tau_{kl}$. We define the residual $f_k^r = f_k - f_k^B$. Starting with the exact initial condition (zero error), errors will develop as we evolve the BGK system:

$$\frac{\partial f_k^r}{\partial t} = -\mathbf{v} \cdot \nabla_{\mathbf{r}}(f_k - f_k^B) \tag{B.2}$$

$$+ \frac{q_k}{m_k} \nabla_{\mathbf{r}}(\phi) \cdot \nabla_{\mathbf{v}}(f_k - f_k^B) \tag{B.3}$$

$$+ \frac{1}{m_k} \sum_l \int \nabla_{\mathbf{r}}(U_{kl}) \cdot \mathbf{v}(f_{kl} - f_k^B f_l^B) \, \mathrm{d}\mathbf{r}' \mathrm{d}\mathbf{v}' \tag{B.4}$$

$$- \sum_l \frac{f_{kl}^{eq} - f_k^B}{\tau_{kl}}. \tag{B.5}$$

At the initial time, the only error derives from the third and fourth terms in the equation above, but this error will cause the first two terms to become nonzero as time advances. If the third and fourth terms approximately cancel one another, then the rate of error growth will be small, and the approximation will be valid for a significant amount of time. This is true whenever the BGK operator effectively accounts for the collisional effects of the system.

Total mass and momentum are conserved in both the MD and VBGK models. However, while the total energy in the VBGK model will be conserved, this quantity will differ from the total energy in the MD system. This difference occurs

because the BGK approximation introduces an error in the initial value of the potential energy. The exchange of energy between kinetic and potential forms will also be incorrect. Indeed, the residual in the potential energy is given by

$$PE^r = \frac{1}{2}\sum_{k,l}\int U_{kl}(f_{kl} - f_k^B f_l^B)\,\mathrm{d}\mathbf{r}\mathrm{d}\mathbf{v}\mathrm{d}\mathbf{r}'\mathrm{d}\mathbf{v}'. \tag{B.6}$$

Thus, neither the kinetic energy nor the potential energy in VBGK models will evolve in a way consistent with MD.

An additional error is incurred in the HMM formulation; $\tau_{kl}$ is not optimal throughout each time step, nor perhaps even after updating, because of statistical noise. The resulting algorithm will perform necessarily worse than one with an optimal theoretical $\tau_{kl}$.

## Appendix C. Entropy computation

We select $\tau_{kl}$ by matching the rates of change of the $H_k$ in both the MD and VBGK models. Conveniently, this choice to match rates isolates the effects of the collisional terms and decomposes into species-species interactions naturally in both physical models.

### C.1. $dH_k/dt$ in molecular dynamics

Consider an MD simulation domain that is embedded within the finite-volume cell at $\mathbf{r}$:

$$H_k^{MD} = \int \langle N_k\rangle \log(\langle N_k\rangle)\,\mathrm{d}\mathbf{r}\mathrm{d}\mathbf{v}, \tag{C.1}$$

where integration over $\mathbf{r}$ occurs over the MD domain. We assume that the distribution is spatially homogeneous in the FV cell; thus, $N_k$ here corresponds to only the velocity Klimontovich distribution $N_k = \sum_{i\in S_k}\delta(\mathbf{v}-\mathbf{v}_i)$, and the resulting $\mathbf{v}$ integral is multiplied by the volume $V_{MD}$ of the MD cell. We can use the definition of the delta function to evaluate this integral:

$$H_k^{MD} = \left\langle V_{MD}\sum_{i\in S_k}\log(\langle N_k(\mathbf{v}_i)\rangle)\right\rangle. \tag{C.2}$$

This is not a typical expression for the Boltzmann entropy, so it is worthwhile to explore it. First, we note the intuition that a particle contributes negatively to $H_K^{MD}$ if it has a velocity that is unlikely, on average. That is, the more particles that are found consistently in the tails of the distribution, the larger the entropy.

To take the time derivative of $H_k^{MD}$, we return to the integral formulation so that we can again take advantage of the delta function property:

$$\begin{aligned}\frac{dH_k^{MD}}{dt} &= V_{MD}\left\langle\int\frac{\partial N_k}{\partial t}(\log(\langle N_k\rangle)+1)\,\mathrm{d}\mathbf{v}\right\rangle\\ &= V_{MD}\left\langle\sum_{i\in S_k}\int\frac{\mathrm{d}\mathbf{v}_i}{dt}\delta(\mathbf{v}-\mathbf{v}_i)\cdot\nabla_{\mathbf{v}}(\log(\langle N_k\rangle))\,\mathrm{d}\mathbf{v}\right\rangle\\ &= V_{MD}\left\langle\sum_{i\in S_k}\frac{\mathbf{F}_i}{m_k}\cdot\nabla_{\mathbf{v}}(\log(\langle N_k\rangle))|_{\mathbf{v}=\mathbf{v}_i}\right\rangle,\end{aligned} \tag{C.3}$$

where $\mathbf{F}_i$ is the force on particle $i$ due to its interactions with every other particle in the MD domain. In reality, the entropy production in the cell depends also upon the force interactions between ions inside the cell and those outside it. However, because we consider only the collisional aspects of entropy production, which are local, we can disregard these interactions.

The force exerted on all particles of species $k$ can be decomposed by species using

$$\sum_{i\in S_k}\mathbf{F}_i = \sum_l\sum_{\substack{i\in S_k\\ j\in S_l}}\mathbf{F}_{ij},$$

where $\mathbf{F}_{ij}$ is the force exerted on particle $i$ by particle $j$. This species-wise decomposition allows us to specify interspecies relaxation times $\tau_{kl}$ individually.

Finally, note that we initialize the MD simulation with $\langle N_k\rangle = f_k$ and assume that kinetic distribution functions do not change significantly during the MD simulation. Thus, we replace $\langle N_k\rangle$ with $f_k$ in this calculation, as the distribution should not have moved significantly from its initial state. Therefore, the rate of change of $H_k$ in MD is calculated as

$$\frac{dH_k^{MD}}{dt} = V_{MD} \sum_l \frac{dH_{kl}^{MD}}{dt},$$
$$\frac{dH_{kl}^{MD}}{dt} = \left( \sum_{\substack{i \in S_k \\ j \in S_l}} \frac{\mathbf{F}_{ij}}{m_k} \cdot \sum_{i \in S_k} \nabla_{\mathbf{v}} (\log(f_k))|_{\mathbf{v}=\mathbf{v}_i} \right). \tag{C.4}$$

If $f_k$ is a drifting Maxwellian distribution of the form

$$f_k = A_k \exp\left\{ -\frac{m_k |\mathbf{v} - \mathbf{u}_k|^2}{2T_k} \right\},$$

then the rate of change of the entropy is:

$$\frac{dH_k^{MD}}{dt} = -\frac{V_{MD}}{T_k} \sum_l \left\langle \sum_{\substack{i \in S_k \\ j \in S_l}} \mathbf{F}_{ij} \cdot (\mathbf{v}_i - \mathbf{u}_k) \right\rangle. \tag{C.5}$$

We recover the classical result that the rate of change of the entropy is proportional to the inverse of the temperature. Furthermore, summing this quantity over species results in

$$\frac{dH^{MD}}{dt} \leq 0, \tag{C.6}$$

with equality when the system is in thermal equilibrium, which is the result of the H-Theorem in KT.

We record the velocities of and forces on each particle in order to calculate (C.4) at each time step. The quantity is statistically noisy because it is the derivative of a function that is not necessarily smooth. We attenuate the noise by taking a time average, assuming the system is ergodic and that $dH_k^{MD}/dt$ does not change significantly during the MD simulation.

### *C.2. $dH_k/dt$ in kinetic theory*

In KT, the kinetic entropy $H_k$ inside a finite-volume cell is defined as

$$H_k^{KT} = \int f_k \log(f_k) \, \mathrm{d}\mathbf{r}\mathrm{d}\mathbf{v}. \tag{C.7}$$

Here, the spatial integral is over the kinetic finite-volume cell, and $f_k$ is considered to be uniform over each cell. The rate of change of this quantity according the Vlasov-BGK equation can be found by taking the time derivative of each side and substituting in the expression for $\partial f_k/\partial t$:

$$\begin{aligned} \frac{dH_k^{KT}}{dt} = &- \int \mathbf{v} \cdot \nabla_{\mathbf{r}}(f_k)(\log(f_k) + 1) \, \mathrm{d}\mathbf{r}\mathrm{d}\mathbf{v} \\ &+ \int \frac{Z_k e}{m_k} \nabla_{\mathbf{r}}(\phi) \cdot \nabla_{\mathbf{v}}(f_k)(\log(f_k) + 1) \, \mathrm{d}\mathbf{r}\mathrm{d}\mathbf{v} \\ &+ \sum_l \int \frac{f_{kl}^{eq} - f_k}{\tau_{kl}} (\log(f_k) + 1) \, \mathrm{d}\mathbf{r}\mathrm{d}\mathbf{v}. \end{aligned} \tag{C.8}$$

The second integral vanishes by the divergence theorem because

$$\nabla_{\mathbf{v}}(f_k)(\log(f_k) + 1) = \nabla_{\mathbf{v}}(f_k \log(f_k)).$$

The first integral is the transport of $H_k$ by advection; this transport is treated by the Vlasov portion of the Vlasov-BGK equation. Additionally, transport happens on time and spatial scales far exceeding those of an MD simulation. Thus, we consider matching only the "collisional entropy" in BGK (the third integral) with the collisional entropy observed in MD simulations. Because no advection from neighboring cells is included in MD simulations, the MD model does not have an equivalent term, and equation (C.4) corresponds to the collisional entropy in MD.

Let the non-advective rate of change of entropy be denoted $\left(\frac{dH_k^{KT}}{dt}\right)_{\text{coll}}$. Mass conservation causes the second term in $\left(\frac{dH_k^{KT}}{dt}\right)_{\text{coll}}$ to vanish. We can compute the spatial integral assuming uniformity, letting the volume of the finite volume be $V_{KT}$. Thus, we find

$$\begin{aligned}\left(\frac{dH_k^{KT}}{dt}\right)_{\text{coll}} &= V_{KT}\sum_l \left(\frac{dH_{kl}^{KT}}{dt}\right)_{\text{coll}},\\ \left(\frac{dH_{kl}^{KT}}{dt}\right)_{\text{coll}} &= \frac{1}{\tau_{kl}}\int (f_{kl}^{eq} - f_k)\log(f_k)\,\mathrm{d}\mathbf{v}.\end{aligned} \tag{C.9}$$

We seek to choose $\tau_{kl}$ and $\tau_{lk}$ such that equations (C.9) and (C.4) are equivalent.

### C.3. Solving for the relaxation rates

We guarantee that not just the overall rate of $H_k$ between the MD and BGK models matches, but that the contributions to that rate due to each species $l$ also match individually. That is, our matching condition is the following:

$$V_{MD}\frac{dH_{kl}^{MD}}{dt} = V_{KT}\left(\frac{dH_{kl}^{KT}}{dt}\right)_{\text{coll}}, \tag{C.10}$$

for all $k$ and $l$.

In the case of a single-species system, or when computing the intraspecies relaxation rate of a multispecies system, we have only one equation to satisfy. The equilibrium distribution $f_{kk}^{eq}$ does not depend on $\tau_{kk}$, so the matching condition simply becomes

$$\tau_{kk} = \frac{V_{KT}\int (f_{kk}^{eq} - f_k)\log(f_k)\,\mathrm{d}\mathbf{v}}{V_{MD}\frac{dH_{kk}^{MD}}{dt}}. \tag{C.11}$$

For any two distinct species, two of our matching conditions are coupled because of the dependence of $f_{kl}^{eq}$ and $f_{lk}^{eq}$ on $\tau_{kl}$ and $\tau_{lk}$. The necessary matching conditions become

$$\begin{aligned}V_{MD}\frac{dH_{kl}^{MD}}{dt} &= \frac{V_{KT}}{\tau_{kl}}\int (f_{kl}^{eq}(\tau_{kl},\tau_{lk}) - f_k)\log(f_k)\,\mathrm{d}\mathbf{v}\\ V_{MD}\frac{dH_{lk}^{MD}}{dt} &= \frac{V_{KT}}{\tau_{lk}}\int (f_{lk}^{eq}(\tau_{kl},\tau_{lk}) - f_l)\log(f_l)\,\mathrm{d}\mathbf{v}.\end{aligned} \tag{C.12}$$

Though it appears that we have two equations in two unknowns, these equations are linearly dependent when $f_k$ and $f_l$ are Maxwellian distributions with the same bulk velocity. Moreover, the system becomes ill-conditioned when $f_k$ and $f_l$ are nearly at equilibrium. This problem occurs in practice as the initial condition of a temperature-relaxation problem and may be encountered in many other applications of interest. Additionally, the data from MD are often noisy. We handle both of these issues simultaneously by solving the matching conditions only in the least-squares sense. By changing the problem to a nonlinear optimization problem, the system is no longer underdetermined.

The problem is made easier by taking advantage of the fact that $f_{kl}^{eq}$ and $f_{lk}^{eq}$ are nonlinear functions of the ratio $\tau_{kl}/\tau_{lk}$. For a given ratio $\tau_{lk}/\tau_{kl} = \alpha$, we can solve a well-defined *linear* least squares problem for the relaxation rates $\tau_{kl}(\alpha)$ and $\tau_{lk}(\alpha)$. This formulation leaves us with a univariate nonlinear optimization problem to solve for $\alpha$, which we solve using the nonlinear optimization function included in `scipy`. We use the average of the temperature and momentum relaxation ratios $\alpha = n_l/n_k \cdot (1 + m_l/m_k)/2$ as the initial guess for optimization. The algorithm has proven to be robust regardless of initial guess as long as the overall system is far enough from equilibrium that reasonable statistics can be obtained from MD.

## References

[1] L.G. Stanton, M.S. Murillo, Ionic transport in high-energy-density matter, Phys. Rev. E 93 (2016) 043203, https://doi.org/10.1103/PhysRevE.93.043203, https://link.aps.org/doi/10.1103/PhysRevE.93.043203.
[2] J.R. Haack, C.D. Hauck, M.S. Murillo, A conservative, entropic multispecies bgk model, J. Stat. Phys. 168 (4) (2017) 826–856, https://doi.org/10.1007/s10955-017-1824-9.
[3] A.A. Vlasov, The vibrational properties of an electron gas, Phys. Usp. 10 (6) (1968) 721–733.
[4] S. Chapman, T.G. Cowling, The Mathematical Theory of Non-uniform Gases: An Account of the Kinetic Theory of Viscosity, Thermal Conduction and Diffusion in Gases, Cambridge University Press, Cambridge, 1970.
[5] I.I. Klimontovich, Kinetic Theory of Nonideal Gas and Nonideal Plasma, Nauka, Moscow, 1975.
[6] G.F. Bertsch, H. Kruse, S.D. Gupta, Boltzmann equation for heavy ion collisions, Phys. Rev. C 29 (1984) 673–675.
[7] A.V. Bobylev, K. Nanbu, Theory of collision algorithms for gases and plasmas based on the Boltzmann equation and the Landau-Fokker-Planck equation, Phys. Rev. E 61 (2000) 4576–4586.
[8] J.R. Rygg, J.A. Frenje, C.K. Li, F.H. Séguin, R.D. Petrasso, J.A. Delettrez, V.Y. Glebov, V.N. Goncharov, D.D. Meyerhofer, S.P. Regan, T.C. Sangster, C. Stoeckl, Tests of the hydrodynamic equivalence of direct-drive implosions with different D2 and He3 mixtures, Phys. Plasmas 13 (5) (2006) 052702, https://doi.org/10.1063/1.2192759.

[9] H.W. Herrmann, J.R. Langenbrunner, J.M. Mack, J.H. Cooley, D.C. Wilson, S.C. Evans, T.J. Sedillo, G.A. Kyrala, S.E. Caldwell, C.S. Young, A. Nobile, J. Wermer, S. Paglieri, A.M. McEvoy, Y. Kim, S.H. Batha, C.J. Horsfield, D. Drew, W. Garbett, M. Rubery, V.Y. Glebov, S. Roberts, J.A. Frenje, Anomalous yield reduction in direct-drive deuterium/tritium implosions due to 3He addition, Phys. Plasmas 16 (5) (2009) 056312, https://doi.org/10.1063/1.3141062.
[10] C. Bellei, H. Rinderknecht, A. Zylstra, M. Rosenberg, H. Sio, C.K. Li, R. Petrasso, S.C. Wilks, P.A. Amendt, Species separation and kinetic effects in collisional plasma shocks, Phys. Plasmas 21 (5) (2014) 056310, https://doi.org/10.1063/1.4876614.
[11] L. Yin, B.J. Albright, W. Taitano, E.L. Vold, L. Chacón, A.N. Simakov, Plasma kinetic effects on interfacial mix, Phys. Plasmas 23 (2016) 112302.
[12] H.G. Rinderknecht, H. Sio, C.K. Li, A.B. Zylstra, M.J. Rosenberg, P. Amendt, J. Delettrez, C. Bellei, J.A. Frenje, M. Gatu Johnson, F.H. Séguin, R.D. Petrasso, R. Betti, V.Y. Glebov, D.D. Meyerhofer, T.C. Sangster, C. Stoeckl, O. Landen, V.A. Smalyuk, S. Wilks, A. Greenwood, A. Nikroo, First observations of nonhydrodynamic mix at the fuel-shell interface in shock-driven inertial confinement implosions, Phys. Rev. Lett. 112 (2014) 135001, https://doi.org/10.1103/PhysRevLett.112.135001, https://link.aps.org/doi/10.1103/PhysRevLett.112.135001.
[13] P. Amendt, S.C. Wilks, C. Bellei, C.K. Li, R.D. Petrasso, The potential role of electric fields and plasma barodiffusion on the inertial confinement fusion database, Phys. Plasmas 18 (2011) 056308.
[14] M.J. Rosenberg, et al., Investigation of ion kinetic effects in direct-drive exploding-pusher implosions at the NIF, Phys. Plasmas 21 (2014) 122712.
[15] B.E. Peigney, O. Larroche, V. Tikhonchuk, Ion kinetic effects on the ignition and burn of inertial confinement fusion targets: a multi-scale approach, Phys. Plasmas 21 (12) (2014) 122709, https://doi.org/10.1063/1.4904212.
[16] N.M. Hoffman, G.B. Zimmerman, K. Molvig, H.G. Rinderknecht, M.J. Rosenberg, B.J. Albright, A.N. Simakov, H. Sio, A.B. Zylstra, M.G. Johnson, F.H. Séguin, J.A. Frenje, C.K. Li, R.D. Petrasso, D.M. Higdon, G. Srinivasan, V.Y. Glebov, C. Stoeckl, W. Seka, T.C. Sangster, Approximate models for the ion-kinetic regime in inertial-confinement-fusion capsule implosions, Phys. Plasmas 22 (5) (2015) 052707, https://doi.org/10.1063/1.4921130.
[17] S. Atzeni, A. Schiavi, F. Califano, F. Cattani, F. Cornolti, D. Del Sarto, T. Liseykina, A. MacChi, F. Pegoraro, Fluid and kinetic simulation of inertial confinement fusion plasmas, Comput. Phys. Commun. 169 (2005) 153–159, https://doi.org/10.1016/j.cpc.2005.03.036.
[18] T.E. Itina, J. Hermann, P. Delaporte, M. Sentis, Laser-generated plasma plume expansion: combined continuous-microscopic modeling, Phys. Rev. E 66 (6) (2002) 066406, https://doi.org/10.1103/PhysRevE.66.066406.
[19] W. E, Principles of Multiscale Modeling, Cambridge University Press, Cambridge, 2011.
[20] W. E, B. Engquist, X. Li, W. Ren, E. Vanden-Eijnden, Heterogeneous multiscale methods: a review, Commun. Comput. Phys. 2 (3) (2007) 367–450.
[21] W. Ren, E. Weinan, Heterogeneous multiscale method for the modeling of complex fluids and micro-fluidics, J. Comput. Phys. 204 (1) (2005) 1–26.
[22] T. Pohl, T. Pattard, J.M. Rost, Kinetic modeling and molecular dynamics simulation of ultracold neutral plasmas including ionic correlations, Phys. Rev. A 70 (2004) 033416.
[23] F.R. Graziani, J.D. Bauer, M.S. Murillo, Kinetic theory molecular dynamics and hot dense matter: theoretical foundations, Phys. Rev. E 90 (2014) 033104.
[24] D. Michta, M. Surh, F. Graziani, Kinetic theory molecular dynamics; numerical considerations, High Energy Density Phys. 9 (4) (2013) 696–701.
[25] W. E, X. Li, Analysis of the heterogeneous multiscale method for gas dynamics, Methods Appl. Anal. 11 (4) (2004) 557–572.
[26] A. Abdulle, A. Nonnenmacher, Adaptive finite element heterogeneous multiscale method for homogenization problems, Comput. Methods Appl. Mech. Eng. 200 (2011) 2710–2726.
[27] A. Abdulle, A. Nonnenmacher, A short and versatile finite element multiscale code for homogenization problems, Comput. Methods Appl. Mech. Eng. 198 (2009) 2839–2859, https://doi.org/10.1016/j.cma.2009.03.019.
[28] P. Le Tallec, J.P. Perlat, Coupling kinetic models with Navier-Stokes equations, in: CFD Review, vol. 2, 1998, pp. 833–855.
[29] A. Hasegawa, Plasma Instabilities and Nonlinear Effects, Physics and Chemistry in Space, Springer-Verlag, Heidelberg, 1975.
[30] R.L. Lysak, C.W. Carlson, The effect of microscopic turbulence on magnetosphere-ionosphere coupling, Geophys. Res. Lett. 8 (3) (1981) 269–272, https://doi.org/10.1029/GL008i003p00269.
[31] R. Gendrin, Effects of heavy ions on microscopic plasma physics in the magnetosphere, in: B. Hultqvist, T. Hagfors (Eds.), High-Latitude Space Plasma Physics, Springer US, Boston, MA, 1983, pp. 415–436.
[32] S. Plimpton, Computational limits of classical molecular dynamics simulations, Comput. Mater. Sci. 4 (4) (1995) 361–364, https://doi.org/10.1016/0927-0256(95)00037-1, Proceedings of the Workshop on Glasses and the Glass Transition: 1 Challenges in Materials Theory and Simulation.
[33] V. Nikolskiy, V. Stegailov, Floating-point performance of ARM cores and their efficiency in classical molecular dynamics, J. Phys. Conf. Ser. 681 (1) (2016) 012049.
[34] T.C. Germann, K. Kadau, Trillion-atom molecular dynamics becomes a reality, Int. J. Mod. Phys. C 19 (09) (2008) 1315–1319.
[35] U.L. Klimontovich, A. Dobroslavsky, The Kinetic Theory of Electromagnetic Processes, vol. 10, Springer-Verlag, Berlin, 1983.
[36] L. Stanton, M. Murillo, Unified description of linear screening in dense plasmas, Phys. Rev. E 91 (3) (2015) 033104.
[37] J. Huba, NRL Plasma Formulary, Naval Research Laboratory, Washington, D.C., 2013.
[38] T. Morse, Energy and momentum exchange between nonequipartition gases, Phys. Fluids 6 (1963) 1420–1427.
[39] M.S. Murillo, Ultrafast dynamics of neutral, ultracold plasmas, Phys. Plasmas 14 (5) (2007) 055702.
[40] G. Bussi, M. Parrinello, Stochastic thermostats: comparison of local and global schemes, Comput. Phys. Commun. 179 (1–3) (2008) 26–29, special issue based on the Conference on Computational Physics 2007.
[41] B. Leimkuhler, E. Noorizadeh, O. Penrose, Comparing the efficiencies of stochastic isothermal molecular dynamics methods, J. Stat. Phys. 143 (5) (2011) 921–942.
[42] M.E. Tuckerman, G.J. Martyna, Understanding modern molecular dynamics: techniques and applications, J. Phys. Chem. B 104 (2) (2000) 159–178, https://doi.org/10.1021/jp992433y.
[43] M. Tuckerman, B.J. Berne, G.J. Martyna, Reversible multiple time scale molecular dynamics, J. Chem. Phys. 97 (3) (1992) 1990–2001.
[44] S. Gottlieb, On high order strong stability preserving Runge-Kutta and multi step time discretizations, J. Sci. Comput. (2005) 105–128.
[45] S. Kulin, T.C. Killian, S.D. Bergeson, S.L. Rolston, Plasma oscillations and expansion of an ultracold neutral plasma, Phys. Rev. Lett. 85 (2) (2000) 318.
[46] T.C. Killian, M.J. Lim, S. Kulin, R. Dumke, S.D. Bergeson, S.L. Rolston, Formation of Rydberg atoms in an expanding ultracold neutral plasma, Phys. Rev. Lett. 86 (17) (2001) 3759.
[47] T.C. Killian, S. Kulin, S.D. Bergeson, L.A. Orozco, C. Orzel, S.L. Rolston, Creation of an ultracold neutral plasma, Phys. Rev. Lett. 83 (23) (1999) 4776.
[48] D. Roehm, R.S. Pavel, K. Barros, B. Rouet-Leduc, A.L. McPherson, T.C. Germann, C. Junghans, Distributed database kriging for adaptive sampling (d2kas), Comput. Phys. Commun. 192 (2015) 138–147.